

THE UNIVERSITY OF CALGARY

An Exploration of the Emergence of Pattern and Form from Constraints
on Growth

by

Holly Dale

A DISSERTATION

SUBMITTED TO THE FACULTY OF GRADUATE STUDIES
IN PARTIAL FULFILLMENT OF THE REQUIREMENTS FOR THE
DEGREE OF MASTERS IN SCIENCE

DEPARTMENT OF PHYSICS AND ASTRONOMY

CALGARY, ALBERTA

September, 2014

© Holly Dale 2014

Abstract

Growing structures are subjects of the space in which they develop. When space is limited or growth is constrained complex patterns and formations can arise. One example of this is seen in the bark patterns of trees. The rigid outer bark layer constrains the growth of the inner layers, resulting in the formation of intricate fracture patterns. An understanding of bark pattern formation has been hampered by insufficient information regarding the biomechanical properties of bark and the corresponding difficulties in faithfully modeling bark fractures using continuum mechanics. Grasstrees, however, have a discrete bark-like structure, making them particularly well suited for computational studies. In this thesis I present a model of grasstree development capturing both primary and secondary growth. A biomechanical model based on a mass-spring network represents the surface of the trunk, permitting the emergence of fractures. This model reproduces key features of grasstree bark patterns which have the same statistical character as trees found in nature. The results support the general hypothesis that the observed bark patterns found in grasstrees may be explained in terms of mechanical fractures driven by secondary growth and that bark pattern formation is primarily a biomechanical phenomenon. Furthermore, I extend the grasstree model to analyze the patterning of discrete elements on the surface of pandanus fruit. Pandanus fruit also exhibit patterns apparently related to fracturing and constraints of space. In this case, the results show that the pattern is likely a result of a higher level mechanisms as opposed to purely biomechanical.

Acknowledgements

First and foremost I would like to thank my supervisors Dr. Przemyslaw Prusinkiewicz and Dr. David Hobill for granting me this opportunity and for their support and guidance throughout my Masters' degree.

Thank you Dr. Prusinkiewicz for allowing me to join your research lab as a summer student during my Bachelor's degree. You have shown me how to use computational models as a tool to understand nature and the experience I have gained is invaluable. Your encouragement and support has allowed me the opportunity to present my work at an international conference for which I am very grateful.

Thank you Dr. Hobill for always taking the time to discuss my research, be it an unscheduled drop in or a conversation that took hours. Your genuine enthusiasm and interest has kept up my motivation and excitement throughout my degree. Thank you for showing me how to analyze my research from a physics perspective, providing me with a greater understanding of my work.

Thank you to Adam Runions for all your time and work on our paper which is presented in the second chapter of my thesis. I greatly appreciate your guidance when I first joined the lab and your patience in helping me learn how to create computer simulations.

I would also like to thank Dr. Christian Jacob for which your class *Biological Computing* allowed me to pursue a new project that has been included in this thesis as the third chapter. Your comments and feedback throughout the project were very helpful and insightful.

Lastly I would like to thank my parents for the endless opportunities you have

provided me. You have always allowed me the freedom and support to follow my desires, from which I have learned and grown so much. Thank you.

Table of Contents

Abstract	ii
Acknowledgements	iii
Table of Contents	v
Abbreviations	xi
Glossary	xii
1 Introduction	1
1.1 The acquirement of pattern and form	1
1.1.1 Emergence	1
1.2 Spatially constrained growth	3
1.3 Organization of thesis	6
1.4 Contributions	7
1.4.1 Co-contributors	8
2 Biomechanics of bark patterning in grasstrees	10
2.1 Introduction	10
2.2 Previous work	14
2.3 Grasstree Simulation	15
2.3.1 Phyllotactic Pattern Generation	15
2.3.2 Growth Simulation	17
2.3.3 Fracture Simulation	20
2.3.4 Visual Presentation of the Model	24
2.4 Statistical Analysis of Observed and Simulated Patterns	24
2.4.1 Data Acquisition	26
2.4.2 Pattern Characterization	28
2.5 Results	29
2.5.1 Quantification of real grasstree patterns	29
2.5.2 Parameter Space Exploration	31
2.5.3 Number of initial fractures	38
2.5.4 Quantitative analysis of simulated patterns	44
2.5.5 Integrative Model	46
2.6 Discussion	49

3	Patterning in the pandanus fruit	52
3.1	Introduction	52
3.2	Model	54
3.2.1	Geometry	54
3.2.2	Growth and fracture model	58
3.2.3	Addition of phalanges into the model	61
3.2.4	Visualization	61
3.3	Results	62
3.3.1	Parameter space exploration	62
3.3.2	Addition of phalanges into the model	64
3.4	Discussion	65
4	Conclusion	67
4.1	Summary	67
4.2	Contributions	68
4.3	Future work	69
	Bibliography	71
A	Ridley’s model of phyllotactic on the grasstree dome	78
B	An exploration of the emergence of form and fractal structure in simple branching models	80
B.1	Introduction	80
B.2	Model	83
B.3	Collision detection	85
B.3.1	Continuous approximation to collision detection	93
B.4	Dormant buds	96
B.5	Self-similarity	100
B.6	Length of longest branch	102
B.7	Underlying Sierpinski gasket pattern	104
B.8	Steps towards a proof by induction	106
B.9	Discussion	113

List of Tables

2.1	Parameter values used in the grasstree model.	25
2.2	Parameter values used in test simulations.	31
2.3	Slope (α) and y-intercept ($\ln a$) for the three linear regressions in Fig. 2.13.	40
2.4	Real and simulated pattern statistics	46
2.5	Percent differences between real and simulated pattern statistics . . .	46

List of Figures

2.1	Young (left) and mature (right) grasstrees.	11
2.2	Section of a grasstree trunk showing two different patterns	13
2.3	Two parastichy directions (red and blue lines) on the trunk of the grasstree. Image courtesy of P. Prusinkiewicz.	14
2.4	Grasstree phyllotaxis model.	16
2.5	Estimation of the parameters and geometry of the phyllotactic pattern	19
2.6	Mass-spring representation of the grasstree bark	21
2.7	Digitized bark patches and statistics characterizing the patches	27
2.8	Three different fracture patterns spanning two regimes.	32
2.9	A 2D parameter space exploration of the simplified model.	34
2.10	Changing the time parameter Δt from 0.01 to 0.0001, producing negligible differences.	35
2.11	Same model different growth rates.	35
2.12	Setting the mass equal to zero does not change the resulting fracture pattern in a significant way.	37
2.13	The dependence of the number of initial fractures, along the circumference as a function of G^2b	39
2.14	A system that usually produces mostly diagonal fractures produces more vertical fractures when the simulation starts with a large number of randomly placed broken springs.	41
2.15	A system that usually produces vertical fractures will produce diagonal ones when a small number of spatially separated fractures are broken before the simulation begins.	42
2.16	Simulated patterns with different parameters and statistics computed for these patterns	45
2.17	Selected images from the grasstree simulation showing various stages of development.	47
2.18	Bark patterns in the simulation compared to those observed in a real grasstree	48
3.1	Pandanus fruit, images from [36].	52
3.2	Pandanus fruit. Larger separations are phalanges and smaller units are carpels.	53
3.3	Black lines show parastichies in the pandanus	55
3.4	Phyllotactic pattern for the pandanus model geometry.	56
3.5	Collision based model for implementing spiral phyllotaxis on a general surface	57

3.6	Phyllotactic arrangement and geometry of the modeled pandanus fruit.	57
3.7	Representation of carpels as masses and the connection between them as springs	58
3.8	An element (red) and the 6 neighbors (blue) that it is in contact with and will be attached to by springs.	59
3.9	How carpel elements were drawn so that straight edges touched neighboring carpels.	62
3.10	Decreasing the growth rate from fast (left) to slow (right).	63
3.11	Left image has a smaller damping constant compared to the right image.	63
3.12	Lower force threshold for breaking, left, to a higher force threshold for breaking, right.	64
3.13	Real pandanus fruit and simulations.	64
A.1	Profile of the generated apical dome	79
B.1	The Cantor set (A) and Koch curve (B). Images from WolframMathWorld [34] and [57], respectively.	81
B.2	Sierpinski gasket. Images from WolframMathWorld [58].	82
B.3	Progression of the Ulam Maltese crosses from top left to bottom right.	83
B.4	3-branch system with the initial 3 branches (light blue) that each attempt to grow 3 more branches (dark blue arrows) at the next iteration.	84
B.5	First and second iteration of the 2-branch system showing how branches collide (A) and then are removed leaving only the branches that have enough space (B).	86
B.6	2-branch system showing different iterations of growth (from top left to the bottom right).	87
B.7	Larger number of iterations for the 2-branch system.	87
B.8	2-branch system with 3 different angle	88
B.9	3-branch system showing different iterations of growth (from top left to the bottom right).	88
B.10	Larger number of iterations of the 3-branch system.	89
B.11	3-branch structure repeated on different scales.	90
B.12	Large number of iterations of the 4-branch system.	90
B.13	5-branch system with precise collision detection produces many interior branches.	91
B.14	2-9-branch systems with collision detection between the branch segments.	92
B.15	Continuous approximation to collision detection. Branches which would have reached the intersection point first, stay and the others are removed.	93

B.16 Rules for continuous collisions.	94
B.17 Different branching systems using a continuous approximation to collision detection.	95
B.18 Different branching systems with dormant buds	97
B.19 Branching systems with dead and dormant buds.	99
B.20 Dead and dormant bud types for the 3 and 4-branch systems.	100
B.21 Dead and dormant buds for 3 and 4-branch systems.	102
B.22 2-branch system showing the length of the secondary branches.	103
B.23 6-branch and 9-branch system showing an underlying Sierpinski gasket.	105

Abbreviations

DNA	Deoxyribonucleic acid
PC	Principal component
PCA	Principal component analysis
SD	Standard deviation
SE	Standard error
RR	Real reticulate
RV	Real vertical
SR	Simulated reticulate
SV	Simulated vertical

Glossary

The definitions provided here are based on Wikipedia entries.

Inflorescence Group or cluster of flowers arranged on a stem. (<http://en.wikipedia.org/wiki/Inflorescence>)

Sympodial The tip of the stem is terminated causing a lateral portion of the stem to take over. The result is a stem that may appear to be continuous but is actually derived from multiple units, as opposed to a monopodial plant whose stems are continuous. <http://en.wikipedia.org/wiki/Sympodial>

Phyllotaxis Arrangement of leaves on a plant stem. <http://en.wikipedia.org/wiki/Phyllotaxis>

Divergence angle Angle at which leaves are placed around the plant stem in a phyllotactic pattern.

Parastichy A conspicuous spiral line along which adjacent organs (leaf bases in this thesis) are arranged into a phyllotactic pattern.

Golden angle	137.508°. http://en.wikipedia.org/wiki/Golden_angle . Divergence angles approximating the golden angle are found in many plants, including grasstrees.
Secondary meristem	Tissue containing cells which allow for lateral growth of the plant to take place. http://en.wikipedia.org/wiki/Meristem
Apex	In this thesis: synonym for the shoot apical meristem (the tissue at the extremity of a shoot that causes its growth in length; it is also the site at which new leaves are initiated).

Chapter 1

Introduction

1.1 The acquirement of pattern and form

Beautiful, elegant and complex patterns and formations abound in nature. We can see them in fanciful cloud formations and intricate snowflakes; in deep fracture formations of tree bark and the wrinkles on the edges of leaves. These patterns are all around us in both biological and inanimate forms and our admiration and observations has lead to the question, how do these formations and patterns develop?

The work I present here is fundamental research that addresses the question of how natural patterns and forms develop. I focus specifically on how constrained growth can lead to the development of form and show how structure can arise emergently through simple dynamical processes. The field of research that my work falls into is in functional structural plant models (FSPM), an interdisciplinary field using computer models to study problems that relate plant form and function.

1.1.1 Emergence

In the biological world, geneticists and developmental biologists have determined the genetic makeup of specific organisms in the hopes of understanding how the organisms develop. One of the model organisms for this research is the fruit fly, *Drosophila*, for which scientists have succeeded in describing links between molecules and developmental functions [2]. Geneticists have also succeeded in The Human

Genome Project, in the scope of which all 20 500 human genes were sequenced [37]. The genetic sequence seemed like a promise of a complete instructional manual for development, one which we could decode to determine exactly how to rebuild an organism. Ultimately, though, gene expression usually only answers part of the question and leaves insufficient information to create an entire organism.

“Rather than being specified by genes alone, elaborate biological structures may arise through simple dynamical mechanisms” - Cho [13].

Philip Ball describes nature as a “self-made tapestry” in his popular trilogy *Shapes, Flow and Branches* [5]. In these books Ball suggests that reductionist theories of genetics alone is not sufficient to explain the formation of biological structures. He proposes that biological structures must harness the pattern-forming mechanisms of the non-living world which is less laborious than a piece-by-piece construction from DNA. The evidence for this postulate is in the often similar appearances of biological and inorganic materials. Similarly, Wolpert et al. has compared the growth of an organism to creating a paper structure through origami [59]. He explains how it would be very difficult to describe the final form of the paper in detail and a much more useful tactic would be to provide instructions on how to fold the paper. These instructions play the role of DNA and the final formation is a combination of instructions and physical interactions among the different parts.

Emergence is the acquisition of structure by a set of smaller components that interact in a way that is not predetermined to produce the structure. The importance and prevalence of emergence in the development of natural structures is evident. Emergent structures are created through interactions as opposed to precisely guided development just as the waves on sand dunes form. Interactions between differ-

ent parts on small scales, like collisions between individual sand particles, can add together to create a larger effect that was not preprogrammed into the small interactions but results emergently. This notion dates back to Aristotle who stated, “... the totality is not, as it were, a mere heap, but the whole is something besides the parts...” or, “the whole is greater than the sum of the parts” [3]. The development of *Drosophila* has even been shown to require self-organizing processes despite knowledge of the entire genome [8].

1.2 Spatially constrained growth

When considering how structure and form take place, space (i.e., the area/volume surrounding the structure), a seemingly straightforward concept, can play a significant role. Growing objects consume space by moving into new regions around them and when that space is not available and the growth is spatially constrained, certain formations can be prohibited from forming. From the removal of material that does not fit or the displacement of the material to a new location, though, constraints on growth can also lead to new formations that may otherwise not exist. The idea of spatial constraints driving form has been discussed by Prusinkiewicz and Barbier de Reuille in relation to plant formation [41].

The availability of space has been shown to potentially have a large influence on the development of wavy leaves and flowers. In 2002, and later 2004, Sharon et al. showed how the wrinkling on the edges of leaves and flowers can result from differential growth across the surface of the organ [47] [46]. Initially flat leaves can turn into exceptionally wrinkly and wavy structures by growing much faster along

the edges than the interior. When this happens, the more interior portions of the leaf constrain the exterior parts, preventing the edges from expanding in a planar fashion due to the excess material along the edges that cannot fit in the plane. This excessive differential growth will eventually cause the leaf to break planar symmetry and fold into the third dimension creating waves. Sharon et al. compared wrinkly beet leaves to the edges of a torn plastic garbage bag that produces a cascade of folds due to the material near the edge of the tear being stretched, and therefore producing excess material, compared to the interior portions of the garbage bag. They performed biological experiments where they added a growth hormone on the edges of naturally flat leaves showing how the excess growth will cause flat leaves to develop waves along the boundary [46]. They also created a computer simulation of a rubber like material with differential growth showing how a cylindrical tube that grows faster on the top compared to the bottom will produce a similar folding behavior to flowers that have trumpet like shapes with wrinkles on the edges [46].

In 2010, Prusinkiewicz and Barbier de Reuille looked into how the rules imposed by space can be utilized by developing plants to create diverse formations. Similar to Sharon et al., they also showed how folds in leaves can be produced by differential growth by creating a computational model of exponential growth across the surface of a sheet towards one of the edges. They added buckling directions for the sheet following a fractal curve which produced very similar images to kale leaves.

Similar in some ways to how differential growth can lead to folding, different growth rates can also lead to fracturing. When one part of a system grows more than another such that it imposes tension or stress on another part, fractures can result. An early computational model of fracturing was presented by Skjeltorp and Meakin

in 1988 [49]. They introduced a mass-spring model to simulate an experiment they performed consisting of a drying microsphere monolayer between two pieces of glass. Fractures developed on the monolayer from stresses induced by the attachment to the glass that opposes the change in positions of the microspheres as the layer shrinks in size. Their computational model consisted of a triangular mesh of masses connected by springs with a rest length corresponding to the length of the springs when the material is dry and the system starting with spring lengths that are larger than the rest length to simulate a stretched material. Each mass was also attached to another mass at its original position that corresponded to the underlying fixed substrate layer that was fixed in position and opposed changes away from the original position. The resulting simulation patterns were similar to the experimental ones, suggesting that fracturing can be modeled as a bi-layered system with different growth rates.

Dried mud fractures are also an example of constrained development through different growth rates. These fractures occur when water evaporates faster from the top layers than the bottom layers, such that the top layer shrinks in size more so than the bottom layers, creating stresses that eventually causes the top layer to fracture. This process has been modeled through computer simulation showing that these patterns can be reproduced using a bi-layered system with different growth rates [21], [22]. Tree bark patterns have also been reproduced using a fracturing model on a cylinder with an outer dead, bark layer constraining the growth of the growing inner live tissue, resulting in the build up of stresses on the surface, leading to fracturing [21], [22], [20].

An intrinsic, and constraining, property of space is described by Aristotle's exclusion principle which states, *no two objects can occupy the same space at the same*

time [4]. This property refers only to macroscopic objects and can impose consequences when this rule is tested in the form of collisions between objects. This rule alone can greatly influence the shape of structures and create complex patterns by guiding structures into free spaces.

When it became possible to use computers to create simple simulations, Ulam studied the emergence of form from collisions between the branches of a simple recursively branching structure in 1962 [55]. He showed how fractal formations can arise with a branching structure that grows iteratively in 90° angles from the previous branch tips if the space is not occupied by another branch or any other branches are not trying to occupy that space. He named this structure after Maltese crosses for its similar appearance. Ulam and Holliday noted some interesting properties about this structure including that every 2^n iterations has only the main branches alive and all other branches are dead.

Snowflake formation has been modeled as a branching structure occupying only empty spaces and forming self-similar patterns [38]. Bacteria colonies also can produce remarkable branching structures through the avoidance of other branches within the structure [35].

1.3 Organization of thesis

This thesis presents an analysis of how spatial constraints on growth can result in form. The main study presented in this thesis is on the biomechanics of bark fractures in the grasstree. Grasstrees have an unusual, discrete, bark-like structure composed of old, dead leaf bases connected by a sticky resin. This bark structure makes the

grasstree particularly well suited for computational studies by taking advantage of the discrete nature of the constituent elements. To study the bark pattern formation, a dynamic model was created capturing the phyllotactic patterning of bases on the cylindrical trunk during primary growth with a biomechanical representation of the trunk surface permitting the emergence of fractures through secondary growth of the trunk's width. The variety of resulting patterns were analyzed and compared statistically to images of real trees.

The grasstree biomechanical model was then extended to examine patterns on the surface of pandanus fruits. Pandanus fruit also has a discrete surface composed of different fruit elements that separate from each other as the fruit grows in radius. The separation of these fruit was modeled as a fracturing process to determine whether or not similar patterns could be reproduced computationally.

Preliminary analysis into fractal formations emerging from collisions between branches is presented as an appendix.

1.4 Contributions

This work has been published in the journal *Annals of Botany*, titled "Modeling biomechanics of bark patterning in grasstrees" as a special issue proceeding from the conference FSPM (Functional-Structural Plant Models) 2013 held in Saariselkä, Finland, June 9-14 2013. I presented this work at that conference and the paper is an expanded version of that presentation. The resulting fracture patterns from the grasstree model, spanning two variants, are similar qualitatively and quantitatively to the bark fractures in images of real grasstrees. This suggests that the grasstree bark

patterning may be a biomechanical phenomenon, resulting from fracturing occurring due to stress buildup in the bark layer. An initial physical analysis of the different fracture patterns has been made, showing how the energy dissipation rate is related to the system tending towards either elongated or reticulate fracture patterns. The grasstree model was extended to analyze patterning in the pandanus fruit, which was found to require additional rules on fracturing to reproduce similar results, suggesting that the pandanus fruit patterning is not an emergent property of biomechanical fracturing.

Steps towards a proof showing how a Sierpinski gasket formation is always produced in the simple branching model discussed in the appendix is presented. These results illustrate how fractal forms can emergently develop through growth within confined space.

The results presented in this thesis in general support the hypothesis that “space constraints provide a mechanism through which details of form can be elaborated in an emergent fashion” [41].

1.4.1 Co-contributors

The work presented in this thesis was primarily done by myself, but particular portions were contributed by others.

The first study, biomechanics of bark fractures in the grasstree, was done with Adam Runions under the supervision of Dr. Przemyslaw Prusinkiewicz and Dr. David Hobill. Much of the text presented here was taken verbatim from the Annals of Botany paper mentioned above, which was written with the coauthors mentioned above. Some additional material that was not presented in the paper has been

added. The creation of the models presented in this work was done by myself with the exclusion of the dome-like top to the grasstree model, which was created by Adam Runions. Adam also performed the statistical analysis of the bark fracture patterns. For completeness, these sections were included in my thesis. Their authorship is indicated in the text.

Chapter 2

Biomechanics of bark patterning in grasstrees

2.1 Introduction

Xanthorrhoea, commonly known as the grasstree, (Fig. 2.1) is a genus of monocots native to Australia. There are 28 species of grasstrees, some of which, (e.g. *Xanthorrhoea johnsonii*, *glauca* and *latifolia*) develop an arborescent trunk [31]. The main apex of the grasstree periodically produces terminal inflorescences; consequently, vegetative growth is sympodial, with an auxiliary bud taking over further development [24]. The production of an inflorescence can create bends or kinks in the trunk [11] that modify the otherwise cylindrical appearance of the trunk.



Figure 2.1: Young (left) and mature (right) grasstrees. Right image courtesy of P. Prusinkiewicz.

The morphology of grasstrees is adapted to withstand and respond to frequent fires. Their leaves are arranged into dense spiral phyllotactic patterns [51]. During fires, leaves are burnt back to their bases, resulting in the melting of a sticky resin produced by the plant. The solidification of this resin cements the burnt leaf bases together, forming a “stem sheath” [15] or bark-like layer of diamond-shaped leaf bases (Fig. 2.2) that protects the tree from diseases and future fires [31]. The phyllotactic patterning of leaves results in the formation of two different diagonal spirals of leaf bases called parastichies on the cylindrical trunk, Fig. 2.3.

Grasstrees have an unusual characteristic for monocots in that they have a secondary thickening meristem [45]. The secondary thickening meristem leads to the growth of the trunk in diameter, which, as a geometric necessity, increases the dis-

tances between the leaf bases. As a result, the regular lattice of interconnected leaf bases may break into patches that resemble bark patterns observed in other trees. This study focuses on old (hundreds of years) and large (reaching 5m in height) grasstrees in the Mount Kiangarow, Bunya Mountains National Park, Queensland, Australia, in which such bark patterns are common. The dominant pattern consists of highly elongated, predominantly vertical patches of interconnected leaf bases (Fig. 2.2 C). In some trees, a more reticular pattern of patches occurs in certain regions of the trunk (or main stem). In this case the patches are smaller and less anisotropic (Fig. 2.2 B). The difference in patterns appears to be correlated with the observed change in leaf base shape in the two areas (Fig. 2.2 D-H)

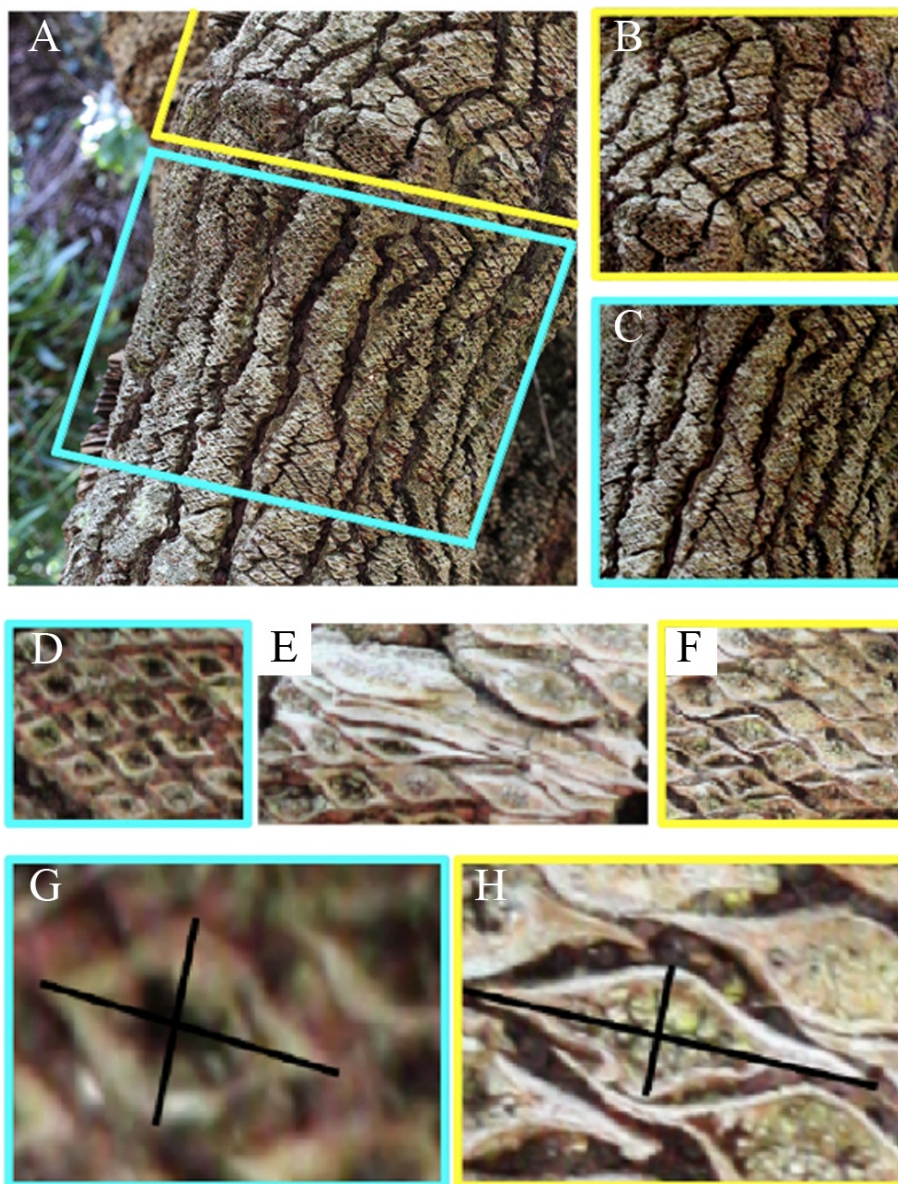


Figure 2.2: Section of a grasstree trunk showing two different bark patterns (A). The yellow box indicates a region with reticulate fractures and the blue box indicates a region with vertical fractures (in the direction of the trunk axis). (B, C) Isolated images of a reticulate pattern (B) and vertical pattern (C). (D-H) Leaf bases in the region with vertical fractures are more equilateral (D, G), whereas leaf bases at the bend of the trunk between the two regions are severely deformed (E) and leaf bases in the region with reticulate fractures are horizontally stretched (F, H). The bend in the trunk is suggestive of an inflorescence site which may have impacted the shape of the bases.

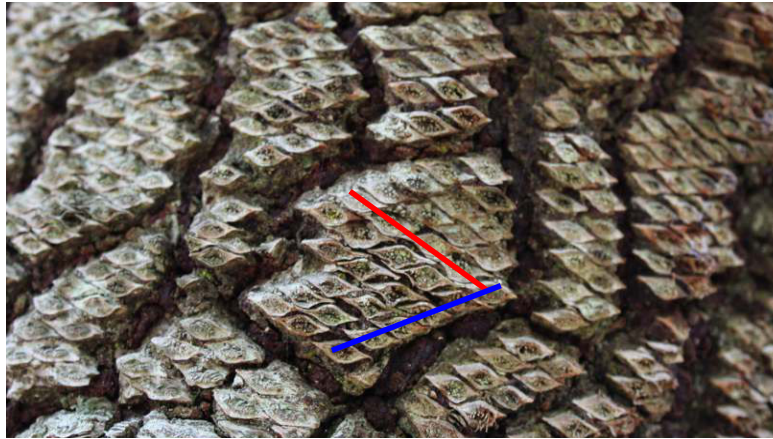


Figure 2.3: Two parastichy directions (red and blue lines) on the trunk of the grasstree. Image courtesy of P. Prusinkiewicz.

This chapter shows how the development of the grasstree bark patterns can be explained as a result of mechanical fractures that emerge in the resin connecting the leaf bases as the trunk grows in circumference. A virtual grasstree model has been created that combines a geometric model of primary and secondary tree growth with a mechanical model of fractures. The natural grid resulting from the phyllotactic arrangement of leaf bases offers a unique opportunity to simulate fractures using a simple discrete model. By changing model parameters, a range of patterns observed in the grasstrees used in the study has been reproduced.

2.2 Previous work

Historically, fractures in different materials have been simulated using both discrete and continuous models. Skjeltorp and Meakin [49] introduced a mass-spring model to simulate fractures in an elastic monolayer under tension. They used a triangular mesh

of masses connected by springs and attached each mass to an underlying substrate layer by another spring. To simulate shrinking in the material, their simulation started with the top layer stretched isotropically (already under tension) and the connecting springs were broken probabilistically depending on the difference between the actual length of the spring and the rest length. To model fractures in tree bark, Federl and Prusinkiewicz [21] adopted the system proposed by Skjetorp and Meakin. They modeled the bark as a bi-layered system with the outer layer of the tree being stretched radially by the inner live tissue. In contrast to the work presented here, they considered the mass-spring model as an (imperfect) discrete approximation of bark that consisted of a homogeneous material. Improving this approximation, Federl and Prusinkiewicz [22] modified their previous model by replacing the masses and springs with a finite-element method. The resulting model produced plausible bark patterns, but the question of whether real bark is adequately approximated as a continuous, homogenous sheet was not addressed.

2.3 Grasstree Simulation

This work is focused on the emergence of fractures that transform the initial phyllotactic arrangement of leaf bases into a structure with a bark-like appearance.

2.3.1 Phyllotactic Pattern Generation

The simplest method for generating the initial arrangement of leaf bases would make use of the geometric characterization of phyllotaxis as a regular lattice on the surface of a cylinder ([19]; [56]; [42]).

The cylindrical phyllotaxy was created according to:

$$\phi = n \cdot \alpha \quad (2.1)$$

$$r = \text{const.} \quad (2.2)$$

$$z = h \cdot n \quad (2.3)$$

where ϕ, r and z are the cylindrical coordinates and n is the ordering number of the element with the first leaf base created starting at 0. Parameter h is the vertical displacement between each new element and α is the divergence angle of the phyllotactic pattern that determines the angular separation between each successive element. The geometry is shown in Fig. 2.4.

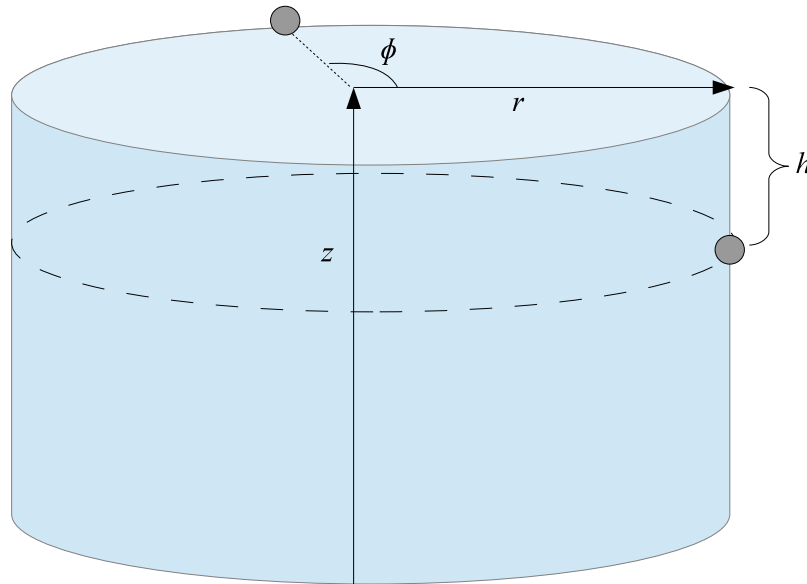


Figure 2.4: Grasstree phyllotaxis model.

A dome-shaped apical part of the trunk that supports leaves was also added

and connected to the cylindrical trunk. The dome was modeled by A. Runions (see appendix A).

2.3.2 Growth Simulation

Primary growth is simulated by increasing the height of the tree linearly as a function of time. Secondary growth is simulated by assuming that the area of the trunk cross section increases linearly with time, and thus the radius increases as the square root of the plant's age. This assumption is loosely motivated by the pipe model [48], according to which a linearly growing number of vascular strands connecting leaves to the base of the tree would result in linear growth in the cross-sectional area of the trunk.

The simulations are limited to older trees, as the data only show bark patterns in such trees. The length and time variables used in the model have been calibrated by assuming that approximately 412.5 leaves grow per year [11] and the trunk typically elongates 10-20mm per year [31]. In the context of these data, one time unit in the model is equivalent to 88.5 days and one length unit corresponds to 0.3 m. The virtual tree starts at a height of 1.62m and reaches a height of 2.52m. This corresponds to a 60 year simulation period with the tree starting at the age of 110 years and reaching 170 years. The force and damping parameter values were unfortunately not able to be approximated into real units due to the limited data from real grasstrees.

According to observations, the divergence angle, α , in young grasstree seedlings (Fig. 2.1) is close to 137.5° , the golden angle value found in many plant species and used in the model as the divergence angle. The radius of the tree trunk during the simulation increased from 11 cm to 29 cm, with the latter value approximating

that observed in trees. Leaf bases were assumed to have an area of approximately 30 mm^2 , which is consistent with the reported size of grasstree leaves [31]. The number of leaf bases that a horizontal line drawn across the trunk intersected was measured and found to be approximately 37 bases (Fig. 2.5E, F), and the angle between parastichies approximated the measured angle of 57° , Fig. 2.5A-D.

Irregularities in the trunk form, possibly related to the sites of inflorescences, were simulated as periodic increases in the trunk diameter (bulging) below the apical dome yielding different leaf base aspect ratios (Fig. 2.5G-I). This was done by increasing the radial position of the affected masses according to a piecewise sinusoidal function taking a single maxima at the site of the bulge and a value of zero away from the bulge. The non-zero portion of the function was a squared sine function with period scaled to match the extent of the bulging region along the trunk, thus guaranteeing a smooth transition to zero at the edges of the functions support.

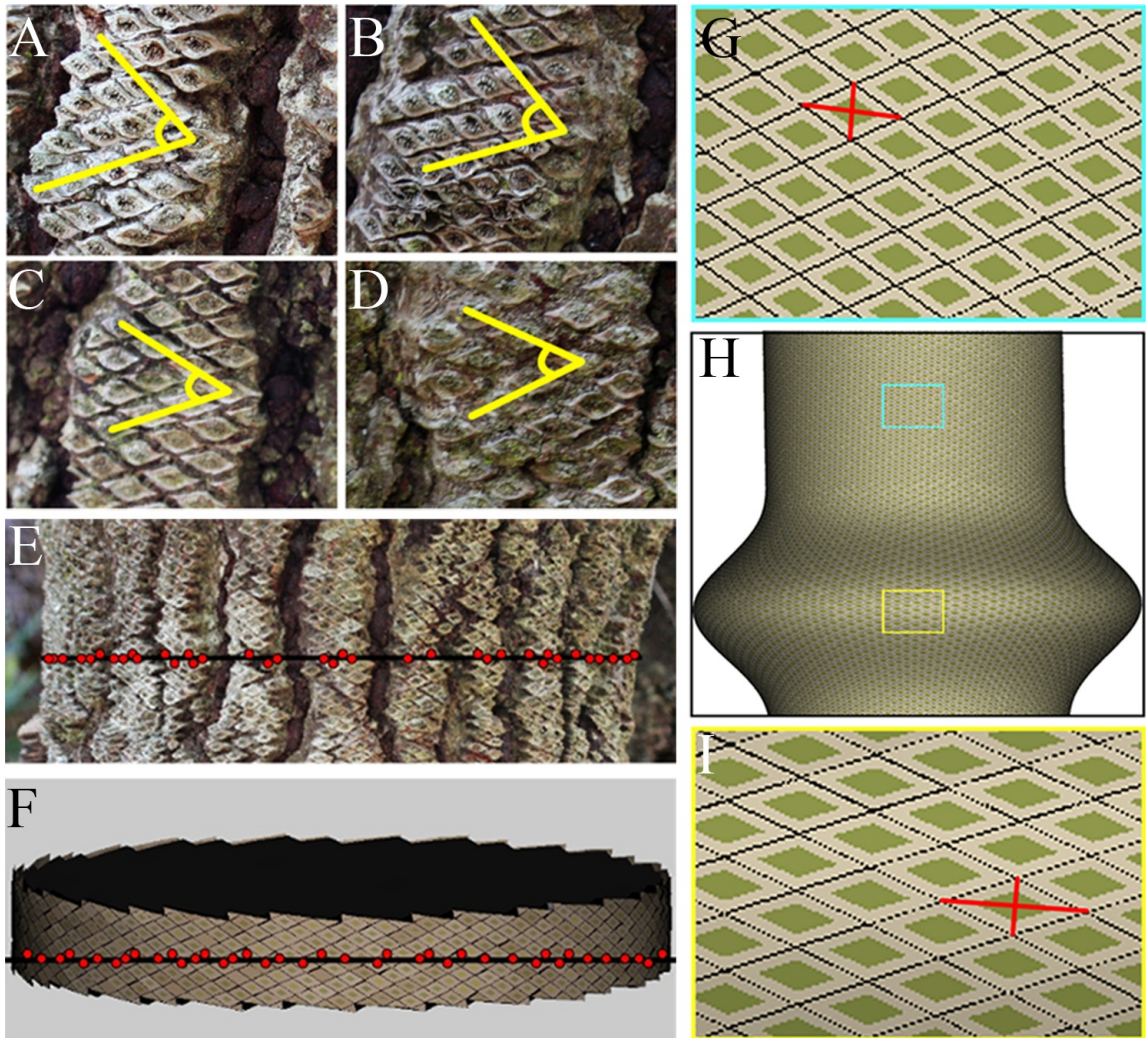


Figure 2.5: Estimation of the parameters and geometry of the phyllotactic pattern. (A-D) Measurements of the angle between parastichies (57) for four different trees/tree sections. (E-F) Comparison of the number of leaf bases intersected by a horizontal line in a grasstree (E) (37) and in the model (F) (40). (H) Calibrated distribution of leaf bases in the regular (blue) and bulged (yellow) segment of the trunk. Leaf bases at the bulge are stretched horizontally (I) compared to regions away from the bulge (G). Note that the lattice spacings (G) correspond to the photo Fig. 2.2G while those shown in (I) correspond to the photo Fig. 2.2H.

2.3.3 Fracture Simulation

Secondary growth pushes leaf bases outwards, which was modeled by gradually increasing the distance of the leaf bases from the tree axis. For the purpose of fracture pattern formation, leaf bases were represented as masses and the resin connections as (Hookean) springs, connecting each base to its four nearest neighbors. Fig. 2.6 A shows the neighboring leaf bases represented as green masses connected by springs. In addition, each mass was connected to its original position on the surface of the trunk by an “anchor” spring, restricting the range of possible displacements of the mass (Fig. 2.6 B). As the tree grew in radius, the springs between leaf bases (and possibly some anchor springs) were stretched. Whenever the tension of a spring connecting two leaf bases exceeded a critical value, f_{max} , the springs would break. Broken springs were removed from the simulation, leading to the formation of cracks, and bark patches were formed by the leaf bases interconnected by the remaining springs.

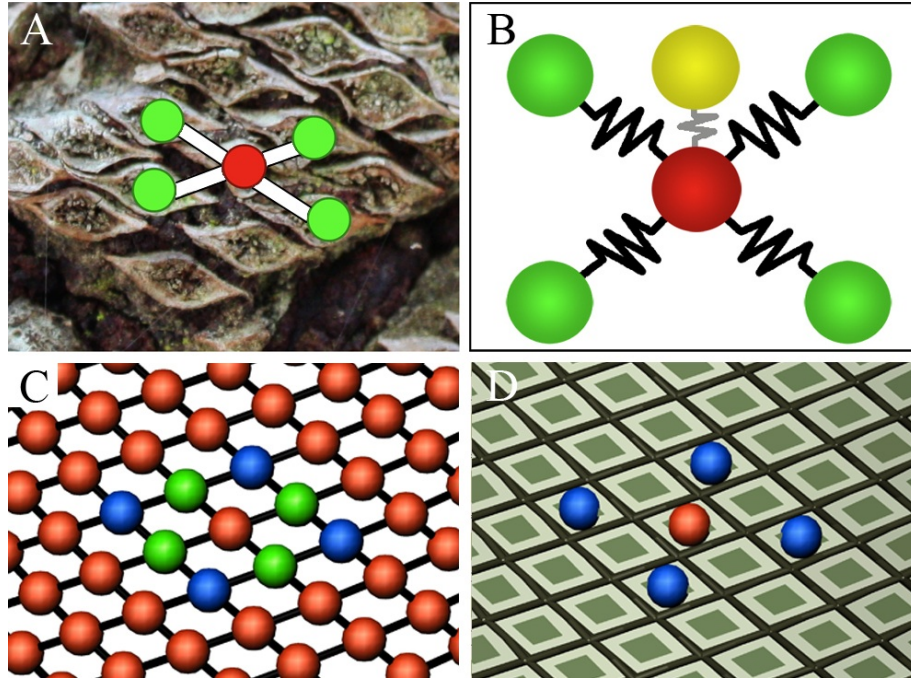


Figure 2.6: Mass-spring representation of the grasstree bark. (A) Leaf bases are approximated as masses (circles) and the resin connections as springs (white connecting lines). (B) Each mass (red sphere) is connected by springs to four neighbors (green spheres), and to an anchoring point (yellow sphere) representing an abstraction of the attachment of the leaf base to the trunk. (C) Masses and springs are arranged into a lattice. (D) The surface of the trunk is partitioned into individual leaf base elements, where the four vertices of each leaf base are placed half the distance between the red mass and a blue mass.

The force with which a spring attached to a leaf base at a point x_p acts on a leaf base q positioned at x_q is given by

$$\mathbf{f}_{q,p} = -k(l_{q,p} - \|\mathbf{x}_p - \mathbf{x}_q\|) \frac{(\mathbf{x}_p - \mathbf{x}_q)}{\|\mathbf{x}_p - \mathbf{x}_q\|}, \quad (2.4)$$

where k is the spring constant. The rest lengths of the springs, $l_{q,p}$, between the adjacent leaf bases were assumed to be equal to the distances between the bases at the time of their transition from the apical dome to the trunk. This implies that leaf bases initiated later in the simulation, when the radius of the tree trunk was larger, and those occurring in the bulging regions, had larger rest lengths. Anchor springs were assumed to have zero rest length, which simplified the above formula to

$$\mathbf{f}_{q,s} = -c(\mathbf{x}_s - \mathbf{x}_q), \quad (2.5)$$

where c is the spring constant and \mathbf{x}_s is the original position of the leaf base on the trunk. The damping force is given by the equation,

$$\mathbf{f}_{q,d} = -b\mathbf{v}_q, \quad (2.6)$$

where \mathbf{v}_q is the velocity of mass q , and b is the damping constant. Due to the physical nature of the system (leaf bases glued by resin), the system was assumed to be over-damped ($b > 2\sqrt{km_q}$, where m_q is the mass of element q).

The total force acting on the leaf base q is the sum of the spring and the damping forces,

$$\mathbf{F}_q = \mathbf{f}_{q,s} + \mathbf{f}_{q,1} + \mathbf{f}_{q,2} + \mathbf{f}_{q,3} + \mathbf{f}_{q,4} + \mathbf{f}_{q,d}, \quad (2.7)$$

where $\mathbf{f}_{q,j}$ ($j=1,2,3,4$) correspond to the springs connecting q to the adjacent bases.

Although grasstree growth is a slow process, numerically it was considered as a dynamic system. The positions of each of the masses in the system were simulated by solving the system of differential equations

$$m_q \frac{d\mathbf{v}_q}{dt} = \mathbf{F}_q \quad (2.8)$$

$$\frac{d\mathbf{x}_q}{dt} = \mathbf{v}_q \quad (2.9)$$

using the Euler-Cromer method [25]:

$$\mathbf{v}_q(t + \Delta t) = \frac{\mathbf{F}_q(t)}{m_q} \Delta t + \mathbf{v}_q(t) \quad (2.10)$$

$$\mathbf{x}_q(t + \Delta t) = \mathbf{v}_q(t + \Delta t) \Delta t + \mathbf{x}_q(t). \quad (2.11)$$

The mass index q runs from $q=1$ to $n(t)$, where $n(t)$ is the total number of leaf bases present in the trunk at a given time. Δt is the time step used for integration and chosen so that the system is able to reach convergence. Each mass q was constrained to lie on the surface of the trunk. This constraint is enforced using the equation

$$\mathbf{x}_q(t) \rightarrow \mathbf{C} + r_i + G\sqrt{t} \frac{(\mathbf{x}_q(t) - \mathbf{C})}{\|\mathbf{x}_q(t) - \mathbf{C}\|}, \quad (2.12)$$

where \mathbf{C} is the position along the trunk axis at the height of leaf base q , r_i is the initial radius of the trunk, and G controls the rate of secondary growth. The anchor points that connect leaf bases to the trunk were constrained to the trunk surface in the same manner. Parameter values used in the model are summarized in Table 2.1.

The real parameter values are presented for reproducibility of results and real world values were mapped to model values when possible.

2.3.4 Visual Presentation of the Model

For visual completeness, leaves were incorporated into the model. Leaves were modeled as generalized cylinders with the cross-section decreasing towards the endpoints. The shape and size of the leaf bases were calculated so that the mesh of masses and springs completely partitioned the surface of the trunk into rhomboids (Fig. 2.6C and D). Leaf bending due to gravity was approximated by gradually turning the leaves downwards along its axis [42]. As the leaves aged, they turned brown and to simulate the role of a forest fire, the majority of the older leaves were eventually removed, leaving only the leaf bases.

2.4 Statistical Analysis of Observed and Simulated Patterns

30 photographs of grasstrees (taken on Mount Kiangarow, Queensland, in December, 2009) were analyzed and certain segments of their trunks were magnified. The bark patterns were clearly visible in most trees, but the individual patches were often partially weathered or covered by an outgrowth of mosses or lichens, which made the precise identification and the recording of individual leaf bases difficult. Consequently, different areas of a single tree have been focused on, in which all bases are remarkably visible. These results have been complemented with an analysis of the distribution of bases and fractures. The statistical analysis was performed by A. Runions.

Table 2.1: Parameter values used in the grasstree model.

Parameter	Symbol	Value
Force threshold for breaking in the straight sections of the trunk	f_{max} - straight	0.005 force units
Force threshold for breaking in the bulging sections of the trunk	f_{max} - bulge	0.006 force units
Initial radius	r_i	0.35 (10 cm)
Vertical displacement for the initial cylindrical trunk	h	0.00012 (0.036 mm)
Index offsets to neighboring masses (green masses in Fig. 2.5)		$\pm 55, \pm 89$
Index offsets to masses used to partition the surface into leaf bases (blue masses in Fig. 2.5C, D)		$\pm 34, \pm 144$
Time step	Δt	0.01 (21 hours)
Elasticity constant for neighboring springs	k	1.0 force/distance units (1.3 force/m)
Elasticity constant for secondary growth springs	c	0.03 force/distance units (0.1 force/m)
Damping constant	b	2.0 force/velocity units
Constant for secondary growth on the straight sections	G - straight	0.04 distance/(time units) ^{1/2}
Constant for secondary growth	G - bulge	0.04 (ends) - 0.02(peak of the bulge) in distance/(time units) ^{1/2}
Spring mass	m_q	1.0 mass units

2.4.1 Data Acquisition

The observed grasstree patches (Fig. 2.2 B, C) were digitized manually from the photographs, using custom software devised by A. Runions for this purpose (Fig. 2.7). Positions of leaf bases were specified by placing a point at the centre of each leaf base using a mouse, and recording the (x, y) coordinates of this point in the plane of the image. In order to minimize the impact of projective distortions, only areas of the trunk approximately facing the camera were considered. This approximation was possible, because the horizontal spread of individual patches was much smaller than the diameter of the trunk. The clustering of leaf bases into patches was estimated by visual inspection, with all bases assigned to the same patch indicated by the same point color (Fig. 2.7 A, D). This assignment was straightforward in the case of patches separated by large gaps. Narrow gaps were more difficult to classify, often raising the question of whether small patches were connected to other patches or not. In order to avoid a possible impact of ambiguous patches, these patches were ignored in the analysis.

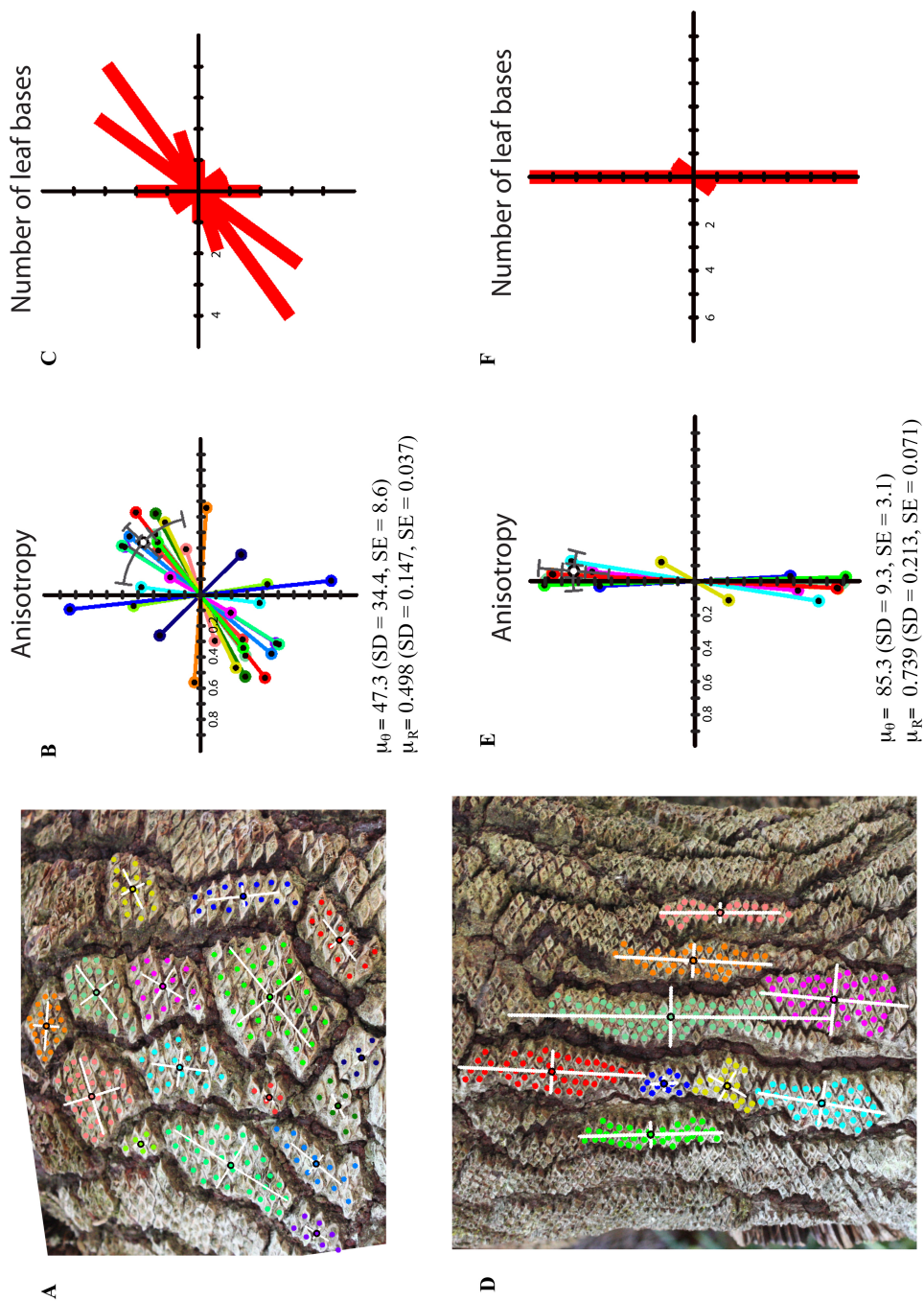


Figure 2.7: Digitized bark patches from two photographs of a grasstree trunk exhibiting reticular patches (A) and vertically oriented patches (D), along with radial plots (B, E) and histograms (C, F) characterizing the patches. Image created by A. Runions.

For simulated data (Fig. 2.16), patches were extracted computationally, based on the graph of connections (unbroken springs) between leaf bases. Each patch corresponded to a single connected component of the graph. Consistent with the method for acquiring experimental data, each patch was mapped into a tangent plane passing through the centroid of the patch and recorded the coordinates of leaf bases in this plane. The analysis focused on the models in which the spread of patches in the horizontal direction was limited, although patches with spreads commensurate with the diameter of the cylinder could also be generated for some parameter values. Furthermore, patches with less than 7 leaf bases were disregarded in order to be consistent with the elimination of ambiguous patches in the analysis of observational data.

2.4.2 Pattern Characterization

The size (in number of leaf bases) of each observed or simulated patch was recorded, and the orientation and anisotropy of each patch was computed by performing Principal Component Analysis (PCA; [28]) on the positions $(x_0, y_0), (x_1, y_1), \dots, (x_k, y_k)$ of leaf bases within a patch. The pairwise covariances of the spatial components of leaf base positions were computed and arranged into a covariance matrix

$$\Sigma = \begin{bmatrix} \text{cov}(X, X) & \text{cov}(X, Y) \\ \text{cov}(Y, X) & \text{cov}(Y, Y) \end{bmatrix} \quad (2.13)$$

From Σ , the eigenvalues of the covariance matrix can be extracted, λ_1 and λ_2 , and their corresponding eigenvectors: α_1 and α_2 . The eigenvectors are the Principal Components (PCs) of the spatial distribution of leaf bases, and the eigenvalues

characterize the portion of the total variance of the point set along each PC. In this setting, the first (larger) PC, λ_1 , describes the primary orientation in which the leaf bases within a patch are distributed. This orientation is visualized as a line aligned with the first PC, passing through the mean of the leaf base positions (see Fig 2.7A and D). The second principal component, λ_2 , characterizes the spread of the leaf bases in the direction orthogonal to the first PC. The ratio

$$A = \frac{\lambda_1}{\lambda_1 + \lambda_2} \quad (2.14)$$

describes the anisotropy of this patch, ranging from $A=1/2$ for a perfectly isotropic patch (the same spread in the first and the second principal direction) to $A=1$ for a perfectly anisotropic patch (all bases aligned in the principal direction) [39]. These values are mapped to the interval $[0,1]$ using the formula $A \rightarrow 2A - 1$ to make the differences in anisotropy more clearly represented in the plots. A similar measure was recently used to quantify the anisotropy of patterns arising in road networks by [17].

2.5 Results

2.5.1 Quantification of real grasstree patterns

The two variants observed in the grasstree, reticulate (Fig. 2.7 A) and vertical (Fig. 2.7 D), have been analyzed statistically. Fig. 2.7 A has 16 digitized patches, and Fig. 2.7 D has 9. Leaf base positions (colored disks), mean position (colored disks with black borders), and principal components (white lines) are shown for each

patch. The same color is used for all leaf bases in a given patch. The radial plots (Fig. 2.7 B, Fig. 2.7 E) show the orientation (angle) and anisotropy (radius) of each patch. Anisotropy values range from 0 to 1, with the increments of 0.1 marked by ticks. The color of each data point matches the corresponding patch in Fig. 2.7 A or Fig. 2.7 D. Numerical values for the mean orientation, ϕ_θ , and anisotropy, ϕ_R , are provided for each plot along with their standard deviation and error. The histograms (Fig. 2.7 C, Fig. 2.7 F) show the orientations of individual patches grouped into 10 bins of 18° each. The radius of each bin shows the number of patches within each bin (3-patch increments are marked).

The mean orientation of the vertical pattern is much steeper, at 85.3° , than the reticulate pattern, at 47.3° , and the reticulate pattern has a much larger range of orientations with a standard deviation (SD) of 34.4° , whereas the vertical pattern has a standard deviation of 9.3° .

The reticulate pattern is more isotropic with an anisotropy value of 0.498 and a standard deviation of 0.147 and the vertical pattern is more anisotropic with a larger anisotropy value of 0.739 with a standard deviation of 0.213.

The histograms (Fig. 2.7 C, Fig. 2.7 F) show a much larger spread of patch orientations in the reticulate pattern than the vertical pattern. The reticulate pattern has a large group of patches oriented in diagonal directions whereas the vertical pattern has a much smaller range of orientations with almost all of them oriented vertically.

2.5.2 Parameter Space Exploration

The effect of the parameters on leaf base patches produced by the model was examined in a simplified setting, with a trunk segment consisting of 3000 leaf bases growing radially as described by eqn. (2.12). An exploration of the model parameters in this setting revealed a range of patterns spanning two extreme regimes. The results are shown in Fig. 2.8 (parameters are given in Table 2.2).

Table 2.2: Parameter values used in test simulations.

Parameter	Symbol	Value
Force threshold for breaking	f_{max} - straight	0.0028 - vertical (Fig. 2.8 A) 0.005 - reticulate (Fig. 2.8 B) 0.008 - diamond (Fig. 2.8 C) in force units
Initial radius	r_i	0.2 (6 cm)
Vertical displacement	h	0.0005 (0.15 mm)
Index offsets to neighboring masses		$\pm 21, \pm 34$
Time step	Δt	0.01 (21 hours)
Elasticity constant for neighboring springs	k	0.4 force/distance units (0.12 force/m)
Elasticity constant for secondary growth springs	c	0.1 force/distance units (0.03 force/m)
Damping constant	b	5.0 force/velocity units
Constant for secondary growth	G	0.014 - vertical (Fig. 2.8A) 0.011- reticulate (Fig. 2.8 B) 0.007 - diamond (Fig. 2.8C) in distance/(time units) ^{1/2}
Spring mass	m_q	1.0 mass units

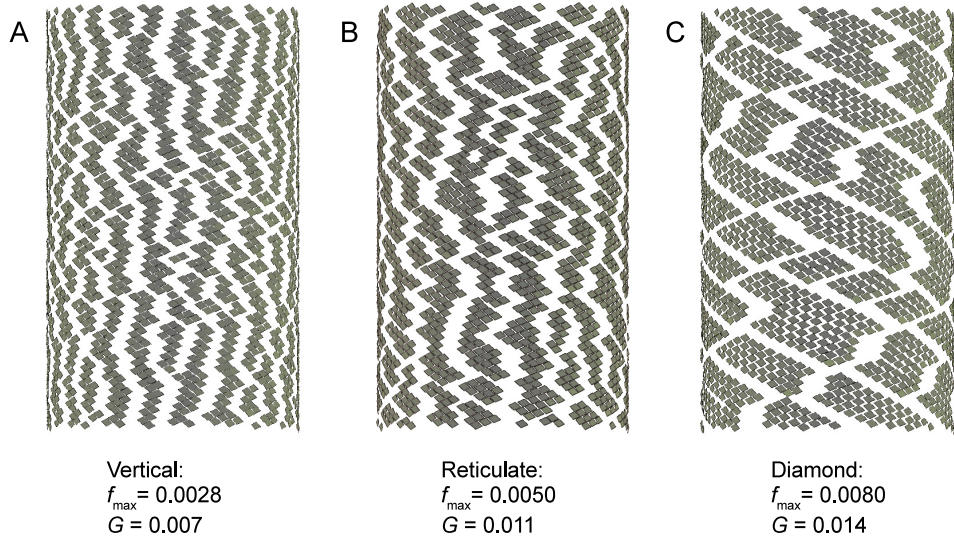


Figure 2.8: Three different fracture patterns spanning two regimes. All images were captured when the simulated trunk attained the same radius. Different fracture patterns are produced by varying the parameters for growth rate G and the force threshold for breaking f_{\max} . The first regime (A) is a vertical pattern, the second regime (C) is a diamond pattern and a third pattern (B) that falls in between the two regimes is a reticulate pattern (B). Parameter values are summarized in Table 2.2

The first regime (Fig. 2.8 A) is characterized by a pattern of patches that are predominantly vertical (along the direction of the trunk axis). Pattern formation begins with a large number of individual fractures between bases connected by the shallower parastichy (which has larger stresses induced by radial expansion) that run along the direction of the steep parastichy. These fractures subsequently connect in zigzag vertical formations through fracturing along the other parastichy direction.

The second regime (Fig. 2.8 C) results from an increase in the threshold for

springs to break (f_{max}), combined with a decrease in the growth rate (G). These changes imply that leaf bases are more likely to be significantly displaced before being divided by cracks into separate patches. The pattern is initiated similarly to the vertical pattern with a small number of fractures along the steep parastichy (between bases connected by the shallow parastichy). These fractures then propagate in the direction of the steep parastichy, producing long diagonal cracks that wind around the trunk and divide the leaf bases into oblique strips. These strips then subsequently split along the shallow parastichy (between bases connected by the steep parastichy), forming numerous diamond-shaped patches. As the trunk grows further, this initial pattern is elaborated hierarchically by the alternate splitting of patches along the parastichies.

Independently varying G and f_{max} has distinct, and continuous effects on the characteristics of the final pattern, (Fig. 2.9). Faster growth rates tend to create more vertical fractures (left column on Fig. 2.9) compared to slower growth rates that tend to produce fractures that run diagonally, along the parastichies (right column of Fig. 2.9). Increasing the force threshold for breaking tends to increase the size of the patches (top row of Fig. 2.9) compare to smaller force thresholds for breaking which have smaller patches (bottom row of Fig. 2.9).

The time step Δt was tested to make sure that it was small enough that the numerical system used (eqns. 2.10, 2.11) could reach convergence and not affect the resulting patterns. Fig. 2.10 shows three of the same models with different Δt values, at the same radius. All three models produce almost identical patterns, suggesting that value used in the model, $\Delta t = 0.01$, allows for the numerical method to converge.

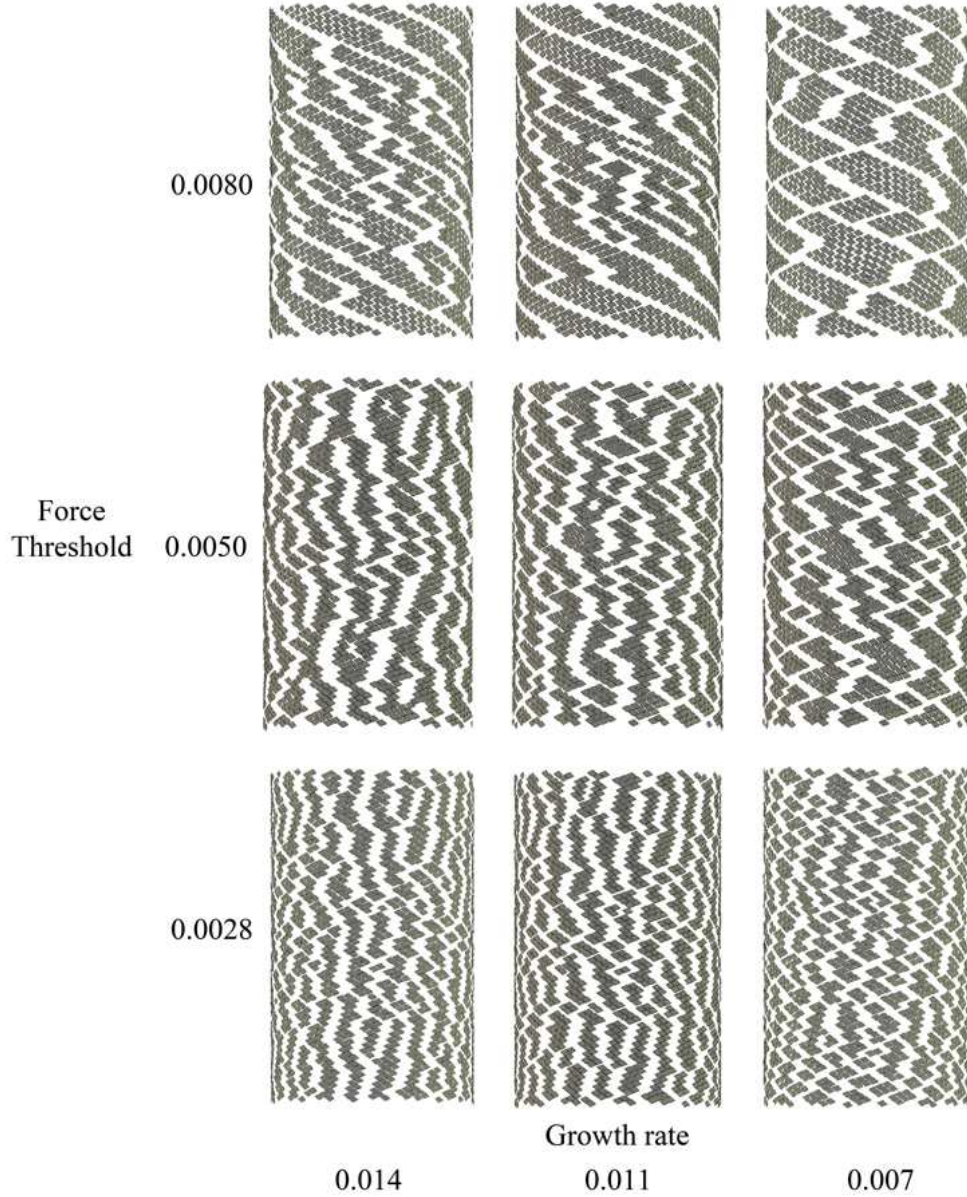


Figure 2.9: A 2D parameter space exploration of the simplified model. The growth rate G is decreased for each column from left to right, but is constant for each column. The force threshold f_{max} is increased for each row from bottom to top, but is constant for each row. The bottom left image is the same as Fig. 2.8 A, the middle image (second column, second row) is Fig. 2.8 B, and the top right image is Fig. 2.8 C. Parameter values used in these models are provided in Table 2.2.

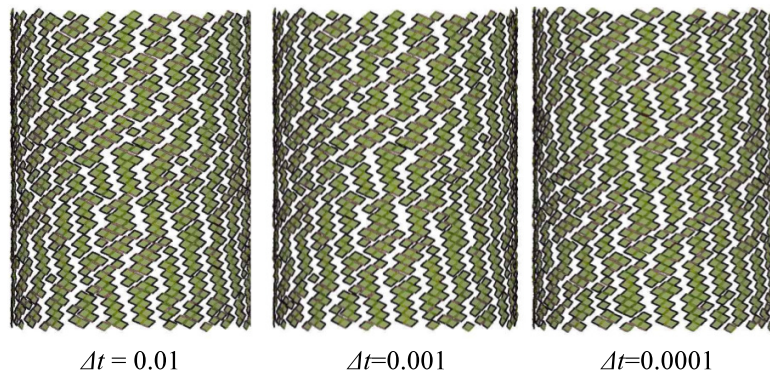


Figure 2.10: Changing the time parameter Δt from 0.01 to 0.0001, producing negligible differences.

The resulting fracture patterns also did not depend critically on the assumed non-linear growth as increasing the trunk radius, rather than cross section, linearly with time produced very similar results, Fig. 2.11.

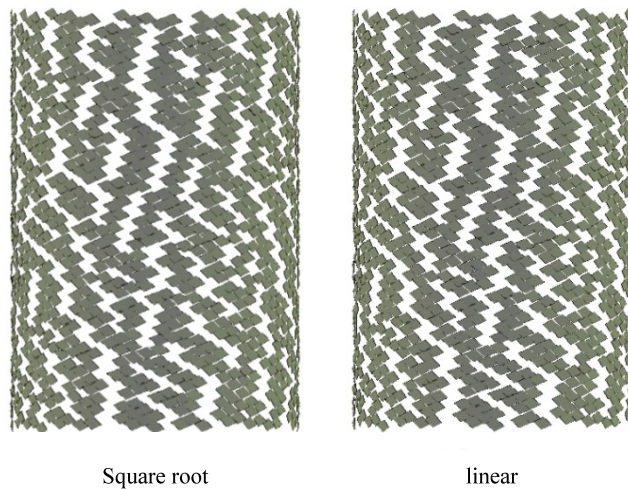


Figure 2.11: Same model with different growth rates, square root and linear growth produce very similar fracture patterns.

Setting the mass to zero was also found to not play a significant role on the resulting patterns, 2.12. The equations of motion were changed in the following manner to have a negligible mass. Setting eqn. 2.8 to zero,

$$m_q \frac{d\mathbf{v}_q}{dt} = \mathbf{F}_q \quad (2.15)$$

$$= -b\mathbf{v} + \mathbf{F}_{springs} \quad (2.16)$$

$$= 0 \quad (2.17)$$

where $\mathbf{F}_{springs}$ is the spring forces between neighboring springs ($\mathbf{f}_{q,j}$ ($j=1,2,3,4$)) and the anchor spring ($\mathbf{f}_{q,s}$). The damping force ($\mathbf{f}_{q,d}$) is equal to $-b\mathbf{v}$. Rearranging the above equations,

$$\mathbf{v} = \frac{\mathbf{F}_{springs}}{b} \quad (2.18)$$

$$\frac{d\mathbf{x}}{dt} = \frac{\mathbf{F}_{springs}}{b} \quad (2.19)$$

$$(2.20)$$

the equation of motion is,

$$\mathbf{x}(t + \Delta t) = \frac{\mathbf{F}_{springs}}{b} \Delta t + \mathbf{x}(t) \quad (2.21)$$

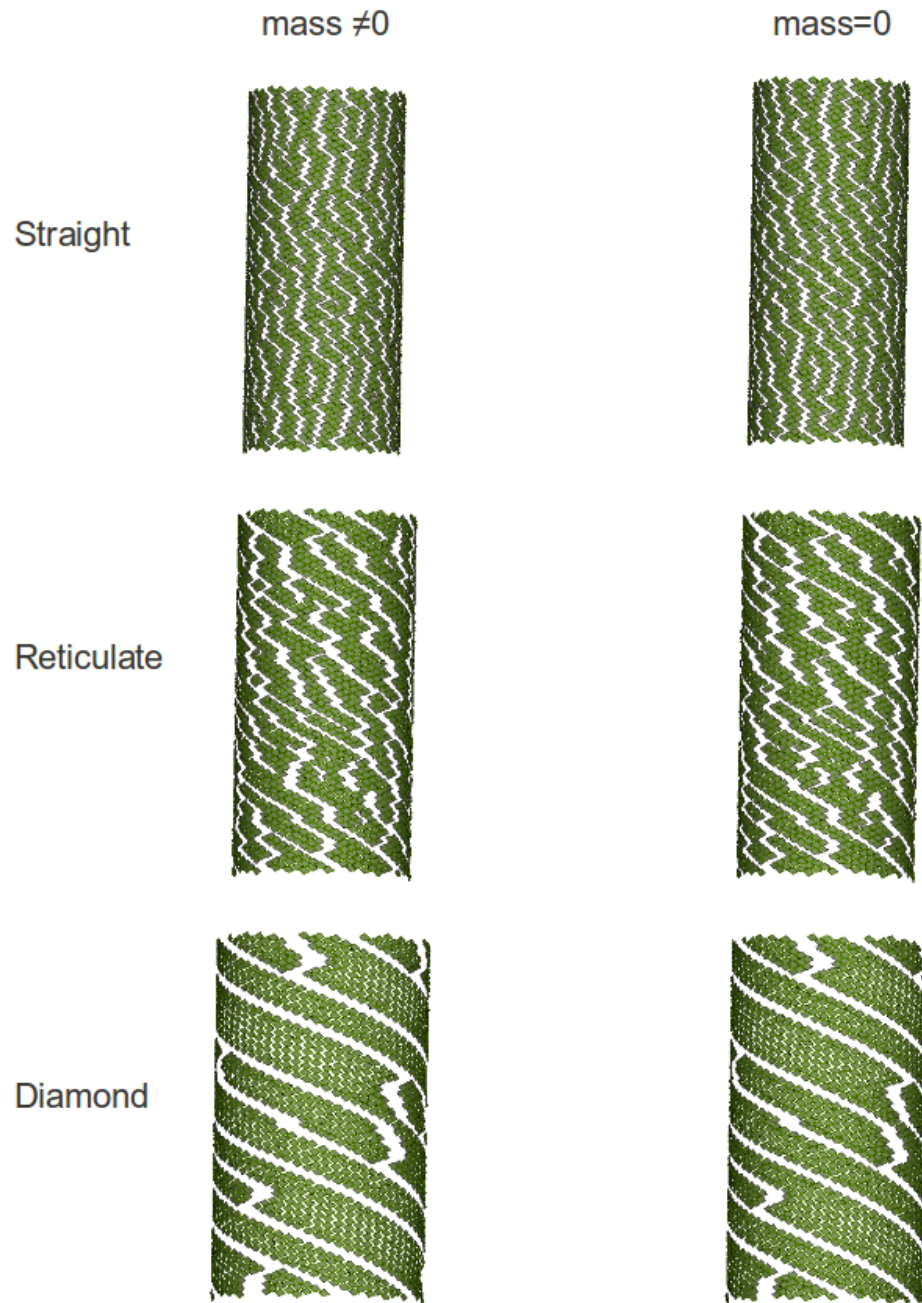


Figure 2.12: Setting the mass equal to zero does not change the fracture pattern in a significant way.

2.5.3 Number of initial fractures

A trend between the number of initial fractures that occurred along a circumference of the trunk and the product of the growth rate squared times the damping constant, G^2b , was found. The number of fractures were counted right after the first round of major fracturing, that follows the stage of initially isolated fractures, where the simulations tend to remain static for a while before any further fracturing takes place (these fracture phases were also noted by Skjeltorp and Meakin [49]). The number of broken springs around various circumferences, of one leaf base thick, were counted and the average was used.

Fig. 2.13 plots the logarithm of the number of fractures n as a function of the logarithm of G^2b . Each plot in Fig. 2.13 is computed for a fixed force threshold for the breaking of the springs. The values used for the growth rates and those for the force thresholds are those given in Fig. 2.9. That is $G = 0.014, 0.011$ and 0.007 , while $f_{\max} = 0.0080, 0.0050$, and 0.0028 . The damping constant is also varied with the values $b = 2.0, 5.0$ and 10.0 where the patterns shown in Fig. 2.9 were all for $b = 5.0$. The straight lines in the log-log plot indicates that the number of fractures seem to obey a a power law relation to G^2b ,

$$n = a (G^2b)^\alpha \quad (2.22)$$

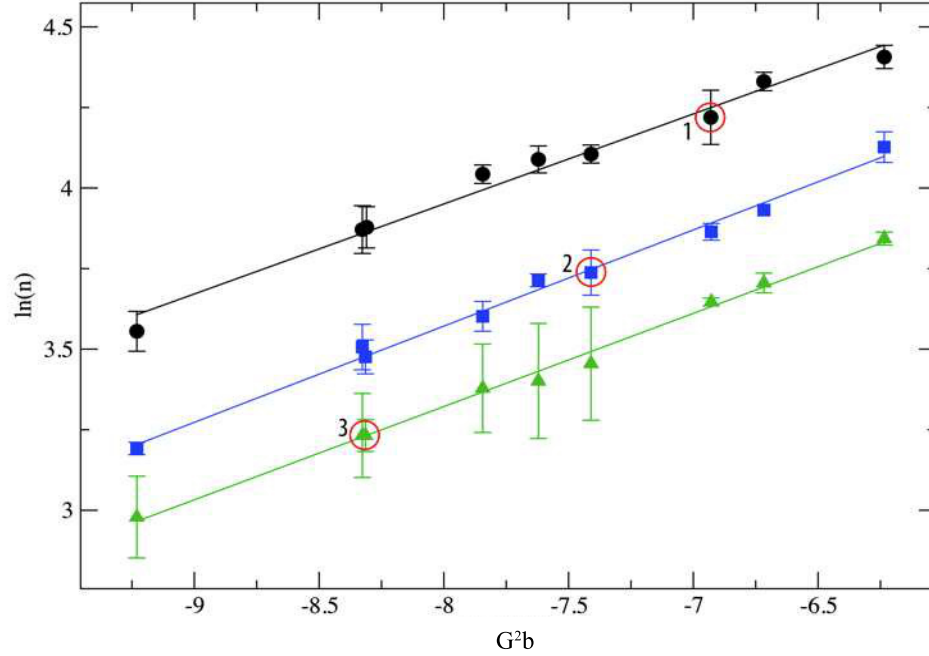


Figure 2.13: The dependence of the number of initial fractures, n , along the circumference as a function of G^2b . The growth rates are $G = 0.014$, 0.011 and 0.007 . The damping constants $b = 2.0$, 5.0 and 10.0 and the force thresholds $f_{max} = 0.0028$ (black circles), 0.0050 (blue squares) and 0.0080 (green triangles). The red circles outline the 3 fracture patterns analyzed throughout the chapter, 1 corresponds to the vertical pattern (Fig. 2.8 A), 2 corresponds to the reticulate pattern (Fig. 2.8 B) and 3 corresponds to the diamond pattern (Fig. 2.8 C). The bottom left side of the plot is dominated by the initiation of diagonal fractures (along the steeper parastichy) and the top right of the plot produces vertical initial fractures. The area between points 1-3 (Fig. 2.13) includes the transition from diagonal to vertical fractures.

The force threshold f_{max} has only a small effect on the slope, since the exponent

in the power law varies by less than ten percent (See Table 2.3). Larger f_{max} values, though, significantly shift the curves downwards towards a lower number of initial fractures compared to higher f_{max} values. The points outlined by red circles in Fig. 2.13 show the three models that have been analyzed throughout this chapter, with circle 1 corresponding to Fig. 2.8 A, circle 2 corresponding to Fig. 2.8 B and circle 3 corresponding to Fig. 2.8 C.

Table 2.3: Slope (α) and y-intercept ($\ln a$) for the three linear regressions in Fig. 2.13.

$f_{max}(\text{forceunits})$	α	a (force·distance/time units)
0.0028	0.27927	485.3
0.0050	0.2985	387.4
0.0080	0.28931	280.5

The number of fractures that initially develop is key in determining whether a system produces vertical or diagonal fractures. When a large number of fractures occurs initially, the fractures tend to connect to each other along both shallow and steep parastichies, forming a vertical zigzag pattern. Alternatively, when a smaller number of fractures occur initially, the fractures can have larger separations and they tend to propagate in the direction of the steeper parastichy.

A system that normally produces diagonal fractures (Fig. 2.14 left) was started with a large number of randomly broken springs throughout the mesh (black lines on the right image of Fig. 2.14) before the simulation began. This caused the system to produce vertical fractures from connecting with the randomly broken ones, Fig. 2.14 middle. Similarly, a model that usually produces vertical fractures (Fig. 2.15 top)

was started with a small number of initial fractures (Fig. 2.15 red dots), with large separations between them, the fractures propagated in diagonal lines along the steep parastichy until they were close enough to connect to each other in vertical lines (Fig. 2.15 bottom). Although the number of initial fractures is not enough to specify the resulting patterns from different points on the graph with the same value of n , the combination of f_{max} and G^2b together show a continuum on Fig. 2.13 from diagonal diamond fractures on the bottom left side of the plot to vertical fractures on the top right. The area between points 1 and 3 is a transition zone from initially diagonal fractures (characteristic of the diamond pattern) to vertical fractures.

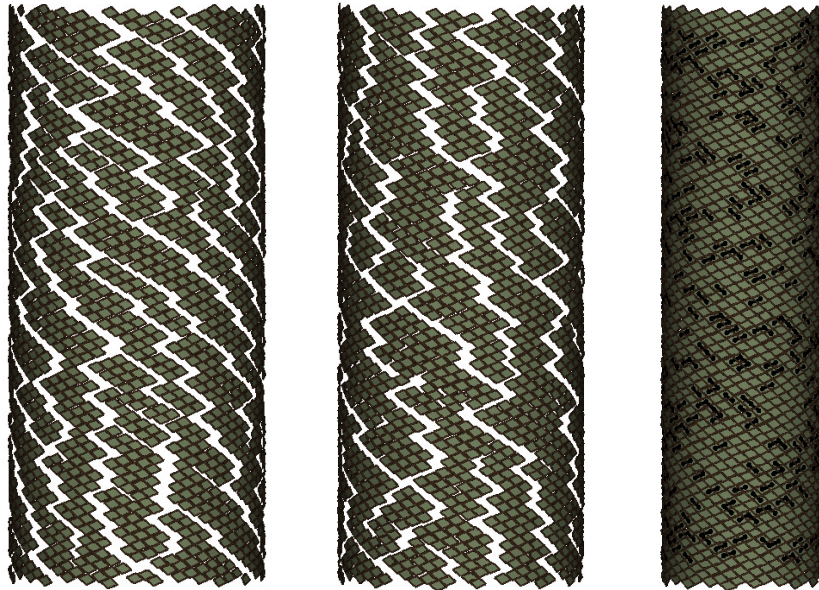


Figure 2.14: A system that usually produces primarily diagonal fractures (left) will produce more vertical fractures (middle) when the simulation starts with a large number of randomly placed broken springs (black lines on right image).

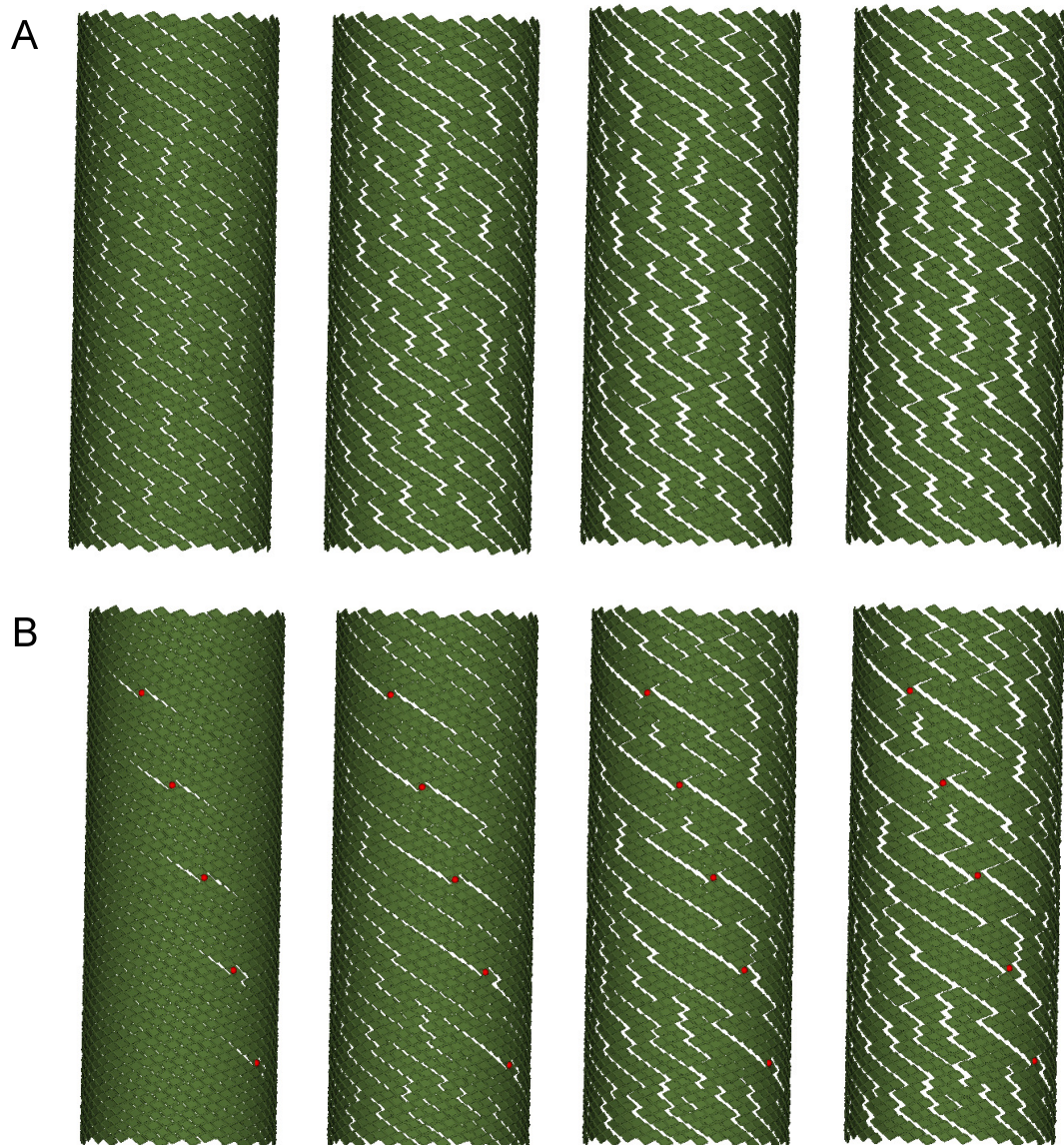


Figure 2.15: Fracture progression (left to right) of a system that usually produces primarily vertical fractures (A) and the same system with 5 initial fractures (B) shown as red dots. The initial fractures in (B) cause the system to form more diagonal fractures as the small number of initial fractures propagate in diagonal lines until they are close enough to connect to other fractures in vertical lines.

It is well known in geophysics and in mechanical engineering that the fracturing of brittle materials depends on the rate at which energy dissipation occurs [12]. It has been shown that larger energy dissipation rates lead to smaller particle sizes, i.e. a greater number of fractures over a fixed size (length, area or volume) object and the particle size exhibits a power law relationship to the energy loss rate. The energy dissipation in the mass-spring system can be solved for a single mass, q ,

$$m_q \frac{dv_q}{dt} = -bv_q - kx_q. \quad (2.23)$$

The total mechanical energy is the sum of the kinetic energy and the potential energy between them,

$$E_q = \frac{1}{2}m_q v_q^2 + \frac{1}{2}kx_q^2. \quad (2.24)$$

The rate of change of energy is

$$\frac{dE_q}{dt} = m_q v_q \frac{dv_q}{dt} + kx_q v_q. \quad (2.25)$$

Replacing $m_q dv_q/dt$ with the right hand side of equation 2.23 yields

$$\frac{dE_q}{dt} = -v_q^2 b. \quad (2.26)$$

The similarity between the value used for the plots, $G^2 b$, and the energy dissipation of a single mass, $v^2 b$, suggests that the power law behavior shown in Fig. 2.13 may be related to the energy dissipation results found by Carpinteri et al [12]. who relate the energy dissipation to the number of fractures.

2.5.4 Quantitative analysis of simulated patterns

Although the diamond pattern of Fig. 2.8 C looks similar to the reticulate pattern found in the real grasstree, Fig. 2.2 B, from the statistical analysis it was shown that a pattern in between the two variants, Fig. 2.8 B, is closer to the reticulate pattern in the real tree.

Radial plots in Fig. 2.16 B, Fig. 2.16 E, Fig. 2.16 H show the orientation and anisotropy. The color of each data point indicates the number of leaf bases in the corresponding patch, according to the color ramp shown on the right hand side of the figure. The histograms (Fig. 2.16 C, Fig. 2.16 F, Fig. 2.16 I) show the number of patches falling into each angular bin.

There is a wide range in the mean orientation of the patches for the different patterns. The vertical pattern (Fig. 2.16 A) has a mean orientation of 83.1° with a standard deviation (SD) of 22.0° , the reticulate pattern (Fig. 2.16 D) has a mean orientation of 50.0° with a SD of 35.5° and the diamond pattern (Fig. 2.16 G) has a mean orientation of 1.2° with a SD of 28.3° . The vertical pattern is nearly straight while the diamond pattern is close to horizontal and the reticulate pattern falls in between.

The anisotropy of the vertical pattern is 0.738 with a SD of 0.173, the anisotropy of the reticulate pattern is 0.577 with a SD of 0.207 and the anisotropy of the diamond pattern is 0.606 with a SD of 0.209. The vertical pattern is the most anisotropic whereas the reticulate pattern is the most isotropic.

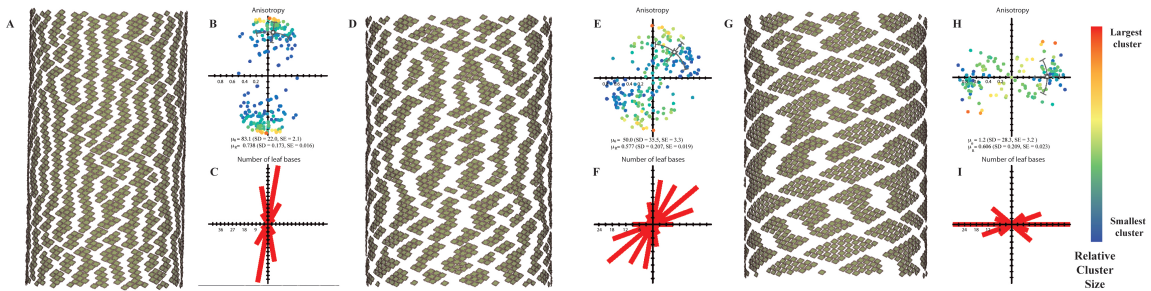


Figure 2.16: Simulated patterns produced by varying the parameters between the two regimes of pattern formation, vertical (A) and diamond (G). Radial plots (B, E, H) show the orientation and anisotropy. Histograms (C, F, I) show the number of patches falling into each angular bin. The number of patches analyzed in each case are 110 for A, 115 for B and 80 for C. Image created by A. Runions.

The simulated and real patterns of the two variants are summarized in Table 2.4. The mean values clearly show that the simulated vertical and reticulate patterns match the corresponding real patterns while being significantly different than each other, although the standard deviations create some overlap. Percent differences between the four patterns are presented in Table 2.5. The percent difference in the mean orientation values show that the real reticulate (RR) and simulated reticulate (SR) patterns are very close (5.5%) and the real vertical (RV) and simulated vertical (SV) patterns are very close (2.6%) while all other are quite different ($\approx 50\%$). The real and simulated vertical patterns have a very small percent different in the anisotropy values (0.1%) where the real and simulated reticulate patterns have a larger percent difference (14.7%) while all other percent values between the patterns are $>24\%$. A quartet analysis is performed in the paper [18], which more rigorously shows how the

simulated vertical and reticulate patterns are closest to the corresponding patterns from the real tree while being relatively distant from each other.

Table 2.4: Real and simulated pattern statistics

	Real vertical (RV)	Simulated vertical (SV)	Real reticu- late (RR)	Simulated reticulate (SR)
Mean orientation	$85.3^\circ \pm 9.3^\circ$	$83.1^\circ \pm 22.0^\circ$	$47.3^\circ \pm 34.4^\circ$	$50.0^\circ \pm 35.5^\circ$
Anisotropy	0.739 ± 0.213	0.738 ± 0.173	0.498 ± 0.147	0.577 ± 0.207

Table 2.5: Percent differences between real and simulated pattern statistics

	RV&RR	RV&SR	RV&SV	SV&RR	SV&SR	RR&SR
Mean orientation	57.3%	52.2%	2.6%	54.9%	49.7%	5.5%
Anisotropy	39.0%	24.6%	0.1%	38.8%	24.5%	14.7%

2.5.5 Integrative Model

Based on the preceding parameter exploration, a model of the entire above-ground part of the grasstree was implemented (Fig. 2.17). The model accounts for primary growth, which includes the arrangement of leaves in a spiral phyllotactic pattern, and secondary growth, which leads to the fractured pattern of the bark-like layer of leaf bases. Bulges were introduced to represent irregularities in the trunk. This

had a secondary effect of producing stretched leaf bases, and a change in leaf base shape similar to that observed in the data from actual grasstrees (Fig. 2.2 B and Fig. 2.2 C). This change in geometry, however, was insufficient to reliably reproduce the different fracture patterns observed. Incorporating the results of the parameter space exploration made it possible to reproduce both elongated and reticulate patterns in the same tree. This was achieved by increasing the force threshold for breaking the springs and decreasing the growth rate in the bulging regions (making the magnitude of the bulge decrease with time). Fig. 2.18 shows a comparison of the bark fracture patterns obtained in the model compared to images of the real tree (same images as Fig. 2.2) showing the two different fracture regimes.



Figure 2.17: Selected images from the grasstree simulation showing various stages of development. The left image has 45 000 leaf base elements and corresponds to an age of 110, the final image contains 70 000 leaf base elements and corresponds to an age of 170 years old. Parameter values are summarized in Table 2.1.



Figure 2.18: Bark patterns in the simulation (left boxes) compared to those observed in a real (right boxes) (the same as in Fig. 2.2 B, C). Regions near bulges or kinks in the trunk (yellow boxes) have reticulate patterns, regions away from the kinks (blue boxes) which have more vertical patterns.

2.6 Discussion

This chapter presents an analysis of the patterns of leaf bases forming the bark-like outside layer of the trunks of old grasstrees. These patterns result from a partitioning of leaf bases, initially arranged into a spiral phyllotactic pattern, into patches. Within each patch, the bases are interconnected by resin. Across the crevices, these connections are missing.

Two variants of these patterns were observed. The first variant is characterized by vertically elongated bark patches and crevices. The second variant is a reticulate pattern of patches and crevices. A principal component analysis was used to characterize both variants quantitatively in terms of the orientation and the degree of anisotropy of their constituent patches. This analysis confirmed the visual observation that patches in the first variant of pattern are highly anisotropic, have a mean orientation close to vertical, and the orientation of individual patches is close to the mean. In contrast, patches in the second variant of the pattern are more isotropic, have a mean orientation of approximately 47° with respect to a horizontal reference axis, and the orientations of individual patches have greater variance ($SD = 34.4^\circ$, compared to $SD = 9.3^\circ$ for the first variant).

Addressing the question of the developmental origin of the observed patterns, a hypothesis that they may result from the mechanical fracturing of the resin between some leaf bases was presented, while the stresses acting on the resin are induced by the expansion of the bark-like layer due to the secondary growth of the trunk. To explore the plausibility of this hypothesis, a simple biomechanical simulation model was constructed. It was shown that for different model parameters, this model

produces patterns that are visually and statistically similar to both the elongated and reticulate patterns observed in real trees.

In particular, decreasing the growth rate and increasing the force threshold for springs to break results in a transition from elongated fractures to a more reticulate pattern. Due to the simplicity of the model, it is difficult to attribute a specific meaning to these parameter changes, but they nevertheless point to physical differences in the two regions as the cause of the different patterns. For example, protrusions on the tree arising from sympodial growth may experience different rates of secondary growth. Furthermore, regions with larger leaf bases may exhibit different fracturing patterns due to a larger area of contact between neighboring bases, leading to a higher force threshold for breaking.

The model has been devised under strong simplifying assumptions. For example, the one-dimensional springs used in the model cannot capture shear stresses that may occur in the resin between leaf bases. Furthermore, all springs in our model are linear (they obey Hooke's law up to the point of breaking), although the grasstree resin may exhibit a more complicated non-linear, plastic and/or viscoelastic [26] behavior. Also, the resin can behave differently at different locations on the tree [9] and vary for different species [7]. Constructing a model of the bark-like patterning in grasstrees based on measured mechanical properties of resin and accounting for the geometry of leaf bases is an open problem, interesting at least from the methodological point of view.

The appeal of using the grasstree as a model for bark-like pattern formation lies in the discrete structure of its layer of leaf bases, which was abstracted as a simple mass-spring model. This model was adequate to support the general hypothesis that

the patterns observed in the grasstree bark-like layer and, perhaps, in the bark of other trees may be explained in terms of mechanical fractures driven by secondary growth. Although the generality of these results is limited by the unusual structure of grasstree bark, it supports the hypothesis that bark pattern formation is primarily a biomechanical phenomenon. From a broader perspective, our results increase the spectrum of morphogenetic phenomena in which biomechanics and properties of space, rather than detailed genetic patterning, play a key role [41].

Chapter 3

Patterning in the pandanus fruit

3.1 Introduction

The grasstree model has been extended to study the pattern formation on the outer surface of pandanus fruit.



Figure 3.1: Pandanus fruit, images from [36].

Pandanus fruit, or screw pine fruit, are native to the Pacific islands, Southeast

Asia and northern Australia. They have a peculiar surface composed of discrete fruit elements that separate from each other as the fruit grows in radius, Fig. 3.1. The discreteness comes from the pandanus fruit being an aggregate fruit, composed of several smaller fruits that develop from separate ovaries [27]. The shape of the fruit is ellipsoid or ovoid due to the flowers of the plant being crowded together in those shapes [32]. The pandanus fruit is made up of tightly bunched fleshy phalanges that are wedge-shaped [53] and the phalanges are composed of 1-15 carpels [32], Fig. 3.2.



Figure 3.2: Pandanus fruit. Larger separations (red outline) are phalanges and smaller units (blue outline) are carpels. Images from <https://flic.kr/p/5v2y9P> [6], outlines were added to the original image

As in the case of the grasstree, the discrete nature of the pandanus fruit makes

it well suited for computational studies. This chapter presents a simulation model of patterning in the pandanus fruit by extending upon the biomechanical fracture model of the grasstree presented in Chapter 2. Fruit fractures, on the skin of the fruit, appear to have formed as a mechanical consequence of surface growth and it has been shown that there exists a potential for intense levels of mechanical stress on the surface of fruits [16]. The fracture model is applied to the patterning of the pandanus fruit to examine whether the fruit patterns may be a result of a similar build up of mechanical stresses on the surface of the fruit, due to radial growth, leading to fracturing between the carpel elements.

3.2 Model

3.2.1 Geometry

The pandanus fruit appears to have a phyllotactic pattern. From observations of images it seems as though the fruit may have parastichies, Fig. 3.3 (black lines). A phyllotactic pattern was used to place the carpels on the surface of the model fruit using the golden angle, 137.5° , as the assumed divergence angle.

A superellipsoid was used to model the shape of the fruit. The placement of the individual carpel elements were determined using the parametric equations in spherical coordinates,

$$x = r \sin(t)^m \cos(T) \quad (3.1)$$

$$y = r \sin(t)^m \sin(T) \quad (3.2)$$

$$z = R \cos(t) \quad (3.3)$$



Figure 3.3: Black lines show parastichies in the pandanus, image from <https://flic.kr/p/bzSMyo> [52].

where

r = semi-minor axis

R = semi-major axis

t = $0 \dots \pi$ - polar angle

$T = n(137.5^\circ)$ - phyllotactic angle

where n is the iteration number or ordering number of the element and m was chosen to be $\frac{2.0}{2.8}$, to produce a similar boxy-ellipse shape to the real fruit. The pandanus model geometry is illustrated in Fig. 3.4.

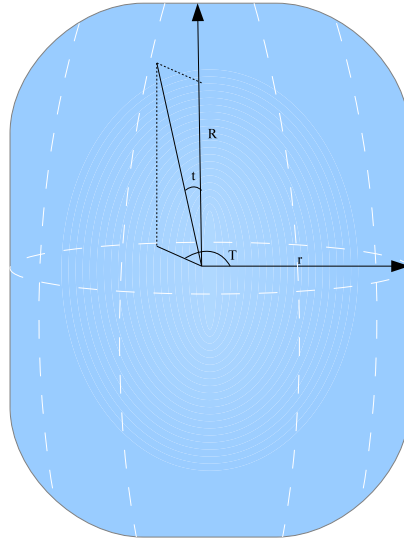


Figure 3.4: Phyllotactic pattern for the pandanus model geometry.

A collision based method was implemented to place the carpel elements on the superellipsoid surface in a phyllotactic pattern [23]. This method allowed for the detection and elimination of collisions between carpels while optimizing the packing. Carpel elements were placed by first determining the angular position, 137.5° away from the previously placed element, and then each element was iteratively brought downwards along the superellipsoid curve at small enough steps so that the element would be placed once it was within a critical distance of another element along the curve. This method is illustrated in Fig. 3.5 (from Fowler and Prusinkiewicz, 1992).

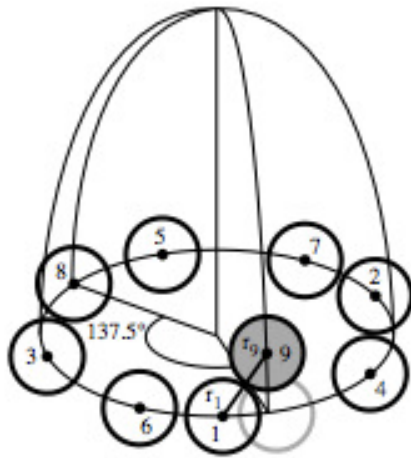


Figure 3.5: Collision based model for implementing spiral phyllotaxis on a general surface, image from Fowler and Prusinkiewicz, 1992 [23].

The resulting shape and phyllotactic arrangement of carpels are shown in Fig. 3.6.

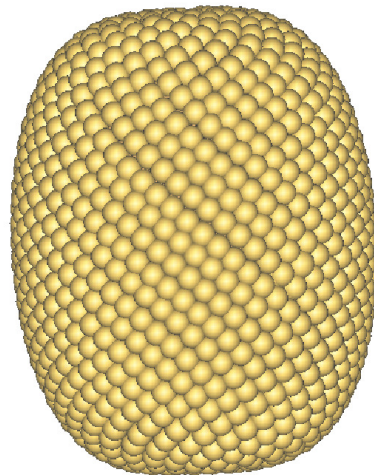


Figure 3.6: Phyllotactic arrangement and geometry of the modeled pandanus fruit.

3.2.2 Growth and fracture model

The mass-spring model, as used in the grasstree mode, motivated by Skjeltorp and Meakin's original model [49], was used to model the surface of the pandanus fruit. The carpels were modeled as masses, connected to each other by springs, Fig. 3.7. The number of nearest neighbors was calculated by determining how many elements were within a given radius, ranging from 1-6 neighbors. An element and its neighbors in the model are shown in Fig. 3.8. Once the neighbors were determined, springs were inserted between the masses, bonding the elements together.

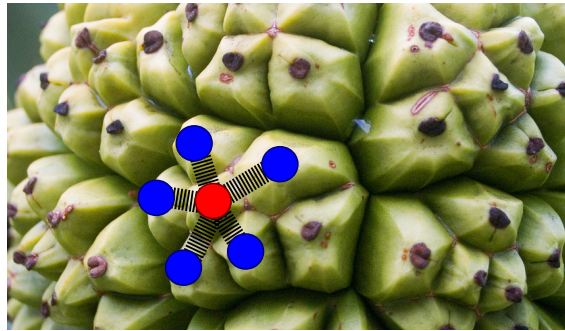


Figure 3.7: Representation of carpels as masses (circles) and the connection between them as springs (dashed lines). The red mass has 5 neighbors that it is in contact with and would be connected to by springs in the model. Image from <https://flic.kr/p/34PUfH> [1] which has been altered by adding the masses and springs on top of the original image.

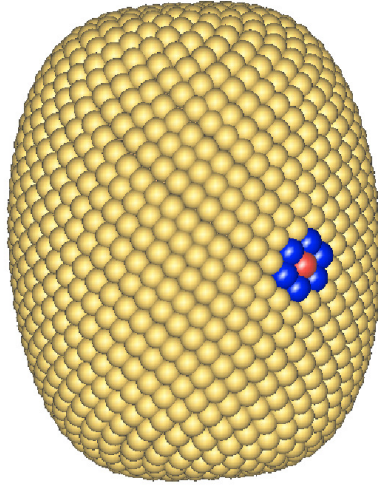


Figure 3.8: An element (red) and the 6 neighbors (blue) that it is in contact with and will be attached to by springs.

Growth in radius of the fruit was simulated using a layer of masses, pulling each mass radially outwards with a spring. The normal direction was found by determining two tangent vectors to the surface by taking the partial derivatives of the parametric equations x , y , and z (eqn. 3.1, 3.2, 3.3) and then taking the cross-product of those vectors,

$$\begin{aligned}
u_{t,x} &= \frac{\delta x}{\delta t} = nr \cos(t) \cos(T) \sin(t)^{n-1} \\
u_{t,y} &= \frac{\delta y}{\delta t} = nr \cos(t) \sin(T) \sin(t)^{n-1} \\
u_{t,z} &= \frac{\delta z}{\delta t} = -R \sin(t) \\
u_{T,x} &= \frac{\delta x}{\delta T} = -r \sin(t)^n \sin(T) \\
u_{T,y} &= \frac{\delta y}{\delta T} = r \sin(t)^n \cos(T) \\
u_{T,z} &= \frac{\delta z}{\delta T} = 0
\end{aligned}$$

The normal vector, \mathbf{N} , is then found from \mathbf{u}_t and \mathbf{u}_T ,

$$\mathbf{N} = \mathbf{u}_t \times \mathbf{u}_T \quad (3.4)$$

In the same manner as the grasstree model, a linear spring force, $\mathbf{f}_{q,j}$, described by Hooke's law, eqn. 2.4, was added for each neighboring mass (j=1...number of neighbors). The other forces include a spring force for the springs attaching each mass to its original position, $\mathbf{f}_{q,s}$, as described by eqn. 2.5, a spring force for growth, $\mathbf{f}_{q,g}$, that pulls each mass radially outwards, as described also by eqn. 2.5 and a damping force, $\mathbf{f}_{q,d}$, as described by eqn. 2.6. The total force on each mass q is then,

$$\mathbf{F}_q = \sum_{j=1}^N \mathbf{f}_{q,j} + \mathbf{f}_{q,s} + \mathbf{f}_{q,g} + \mathbf{f}_{q,d}, \quad (3.5)$$

The Euler-Cromer numerical method, used in the grasstree model, for updating the positions was also used, (eqn. 2.10, 2.11).

As the fruit grows in radius the spring force between masses increases until a critical threshold value is reached and the springs break, creating fractures between the carpel elements. Randomness was added to the model, to break symmetry, in the form of slightly perturbing the initial positions of the elements or by adding small random factors to the spring constants in the system.

3.2.3 Addition of phalanges into the model

The patterning due to the phalanges was also incorporated into some models. This was done by influencing the fracture formation into more clumped forms by adding randomly chosen clump centers throughout the fruit surface. The clump centers were randomly selected carpel elements that simulated the center carpel element in a phalange. These center carpels had higher spring constants and higher thresholds for breaking with the other carpels that it was attached to. Clump centers made it more difficult for fractures to develop between bases connected to the clump centers, and fractures were then more likely to develop between carpel elements of different clump centers or phalanges. The random placement of phalange centers is a rough approximation, as the distribution of phalanges is more likely to be controlled by other means, but this method did allow for a range in the number of carpels that belonged to a phalange, and therefore the size of the phalanges, as it can vary by quite a bit in the real fruit.

3.2.4 Visualization

The carpels were visualized as polygons with edges touching the neighboring carpels that were attached by springs. Fig. 3.9 A shows how this was done where the black

lines represent the mid point between neighboring elements and the resulting form is shown in Fig. 3.9 B. Each carpel was visualized as a wedge shape and an inner core layer was added that grew with the fruit and became visible when fractures appeared.

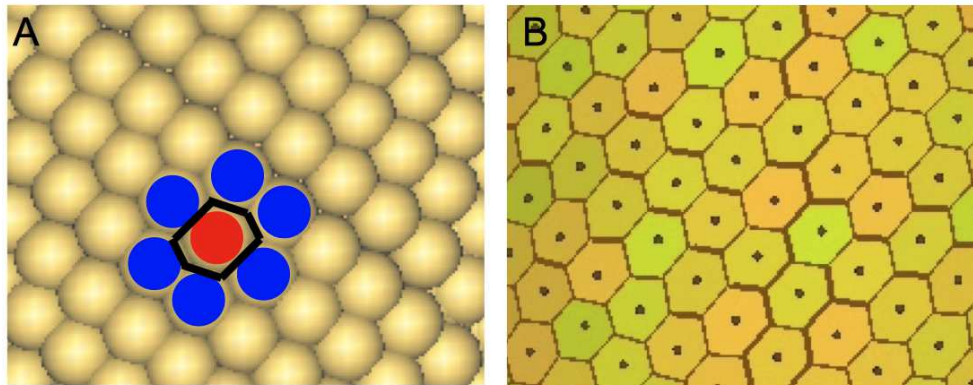


Figure 3.9: How carpel elements were drawn so that straight edges touched neighboring carpels.

3.3 Results

3.3.1 Parameter space exploration

A parameter analysis was performed to analyze the effect of different parameters on the resulting fracture patterns.

Slowing down the rate of growth produced fractures that became larger and straighter, running more so in diagonal lines along the parastichy directions, Fig. 3.10.

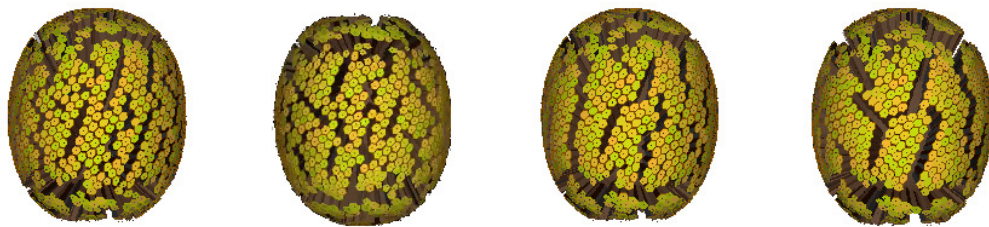


Figure 3.10: Decreasing the growth rate from fast (left) to slow (right).

A smaller damping constant created larger fractures forming island sections, Fig. 3.11.



Figure 3.11: Left image has a smaller damping constant compared to the right image.

Larger force thresholds for breaking produce fewer, larger and straighter fractures that run primarily diagonally, the directions of the parastichies, Fig. 3.12.



Figure 3.12: Lower force threshold for breaking, left, to a higher force threshold for breaking, right.

3.3.2 Addition of phalanges into the model

Adding clump centers to the model to simulate the centers of phalanges produced results that look more like the real fruit, Fig. 3.13 (left) compared to the same simulation without clump or phalange centers (right).



Figure 3.13: Real pandanus fruit (middle) and simulations (left and right). Left image was created with predefined clumping centers and the right image was created without any clumping centers. Image from [30] has been modified by placing the model images over top.

3.4 Discussion

The resulting fracture patterns from the model without phalange centers, Fig. 3.10, 3.11, 3.12, do not look very similar to the patterns seen in the real fruit. The fractures tend to propagate in straighter lines compared to the real fruit. A majority of the fractures appear to be between the bases that are connected by the shallow parastichy, as also observed in the grasstree model, where the stress induced by growth along the normal direction would be the greatest.

The parameter space exploration also produced similar trends found in the grasstree model. Slower growth rates produced more spread out fractures that were straighter and ran primarily in diagonal directions along the parastichies. Smaller damping constants produced larger fractures that formed island-like sections. Higher force thresholds for breaking produced fewer, larger, straighter fractures that ran primarily along the steepest parastichy. These results support the findings from the grasstree analysis and provide a more generic view, as the pandanus model has 3 parastichy directions instead of 2.

Many of the pandanus models had a tendency to fracture horizontally along the top and bottom portions of the fruit and the middle area had more vertical fractures. This is not a phenomenon seen in the real fruit as the real fruit has a strong tendency to form more clumped or island-type fractures. Adding the phalange centers to the model produced patterns that visually appeared to match images of real pandanus fruit better. These results suggest that the phalange structure is important to the resulting pattern. The main patterning mechanism for the pandanus fruit is then likely to be more closely related to the determination of phalanges, for which a

different model of patterning may more accurately capture the structure instead of a purely biomechanical model.

Chapter 4

Conclusion

4.1 Summary

In this thesis, an analysis of pattern and form from constraints on growth is presented. Uniform rules of growth can lead to the development of complex patterns and structures when the growth is constrained and must accommodate for the restrictions. The specific type of constraint that was discussed is the confinement of outwards growth from a non-growing surrounding surface. The outwards grow places tension and force on the confining surface, eventually leading to the development of fractures creating a new pattern and structure on the surface to be analyzed. A biomechanical model of fracturing on discrete structures is presented and applied to the bark fracture patterning in grasstrees and the patterning on the surface of pandanus fruits.

The grasstree offers an analysis of bark fractures on a tree that has a naturally discrete bark-like structure composed of old leaf bases connected by resin. The discrete nature of the bark material makes the grasstree well suited for computational studies. A model of the grasstree including the phyllotactic patterning of leaf bases during primary growth and the increase in trunk width due to secondary growth was created. The trunk surface was represented as a biomechanical structure of masses connected by springs and the growth in the circumference of the trunk lead to the formation of fractures. The resulting fractures produced by the model were able to

capture the two varieties of patterns in the tree both qualitatively and quantitatively through statistical analysis. A preliminary analysis into why changing particular parameters in the model produce different patterns was presented, suggesting that a power law relationship to the number of fractures and the product of the growth rate squared times the damping constant (G^2b) seems to exist.

The grasstree model was then extended to simulate the patterns found on pandanus fruit. The biomechanical model was not able to produce similar patterns from only considering the discrete carpel units but adding phalange centers to the model to guide fracturing produced patterns that were visually more similar to the real fruit emphasizing the importance of the phalange patterning.

4.2 Contributions

From a broad perspective, the work presented here supports the notion that spatial constraints can play a significant role in development as proposed by Prusinkiewicz and Barbier de Reuille [41]. Specifically this thesis has shown that:

1. Bark patterning in the grasstree may be a result of mechanical fracturing.
2. Differences in the bark patterns in the grasstree may be a result of physical differences in the two regions, causing different fracturing behavior as indicated by different dynamical parameters.
3. There seems to be a power law behavior between the product of the growth

rate squared and the damping constant with the number of fractures along the circumference after the first major round of fracturing.

4. Pandanus fruit patterning is likely a result of a higher level mechanism as opposed to purely biomechanical.

4.3 Future work

To further investigate the grasstree bark patterning and help determine whether or not the bark patterns are solely a result of mechanical fracturing, more realistic qualities of the trees could be incorporated into the model. This could be done by modeling the leaf bases as rhomboid shapes instead of point masses to see how the physical structure of the leaf bases may affect the patterning. Modeling the leaf base shapes as physical units may also shed light on the possibility of the different geometric shapes of the leaf bases in the two regions of the tree, producing vertical and reticulate patterns, playing a role in the creation of those patterns. To model the resin more accurately, material properties of the resin from grasstrees could be attempted to be measured. Measuring physical properties of the resin and leaf base material could allow for incorporating more physically realistic parameter values in the model for the force threshold for breaking, the spring constants as well as the damping constant. Adjusting the model to more closely resemble grasstrees would allow for a more in depth understanding of the bark patterning which could lead to new findings about how the patterns are formed or re-emphasize the results

that are presented in this thesis about the grasstree bark patterning. The use of dimensionless parameters in the grasstree model could also be explored so that the number of parameters in the system is decreased. This would capture the essentially different parameters in the system and reduce the parameter space of the model.

A more in depth analysis into the physics behind the development of the fracture patterns would allow for a greater understanding as to why different fracture patterns emerge. The quantity G^2b seems to play a significant role in the resulting pattern as well as the force threshold for breaking. Determining more precisely how these parameters affect the resulting patterns would provide more insight. The power law relationship between the number of fractures and G^2b could also be further analyzed to determine whether or not it is related to the energy dissipation in the mass-spring system.

Further developing the pandanus fruit model could start with observing how the physical bonds between the phalanges and carpels in the real fruit change as the fruit grows in radius. The model presented in this thesis could be further developed to more precisely model phalange sections by placing larger spring constants and force thresholds for breaking between all of the masses within the same phalange instead of just the ones connected to the phalange centers. This would require partitioning the entire surface into phalanges and the major patterning mechanism in the model would then be in dividing the fruit into phalanges, and thus a biomechanical model for pattern formation may not be very relevant and a different biochemical or genetic model may be more suitable.

Bibliography

- [1] R Allen. IMG3344_pandanus. flickr: <https://flic.kr/p/34PUfH>.
- [2] MN Arbeitman, EEM Furlong, F Imam, E Johnson, BH Null, BS Baker, MA Krasnow, MP Scott, RW Davis, and KP White. Gene expression during the life cycle of *Drosophila melanogaster*. *Science*, 297:2270–2275, 2003.
- [3] Aristotle. *Metaphysics*, Book H 1045a 8-10 Electronic edition: eBooks@Adelaide 2007:<https://ebooks.adelaide.edu.au/a/aristotle/metaphysics>.
- [4] Aristotle. *Physics*, 350 BC Electronic edition: eBooks@Adelaide 2007:<https://ebooks.adelaide.edu.au/a/aristotle/physics>.
- [5] P Ball. *Nature's patterns: A tapestry in three parts*. Oxford University Press, 2009.
- [6] L Billeter. Fruit. flickr: <https://flic.kr/p/5v2y9P>.
- [7] AJ Birch and CJ Dahl. Some constituents of the resin of *Xanthorrhoea preissii*, *australis* and *hastile*. *Australian Journal of Chemistry*, 27:331–344, 1974.
- [8] S Bonaccorsi, MG Giansanti, and M Gatti. Spindle self-organization and cytokinesis during male meiosis in asterless mutants of *Drosophila melanogaster*. *The Journal of Cell Biology*, 142(3):751–761, 1998.
- [9] J Bray. Grasstree resin. *Sydney Morning Herald December 15*, page 5, 1905.

- [10] CD Brummitt, H Delventhal, and M Retzlaff. Packard snowflakes on the von Neumann neighborhood. *Journal of Cellular Automata*, 3:57–79, 2007.
- [11] A Bülow-Olsen, J Just, and MJ Liddle. Growth and flowering history of *Xanthorrhoea johnsonii* Lee (liliaceae) in Toohey Forest Queensland. *Physical Review E*, 71:046215, 2005.
- [12] A Carpinteri, G Lacidogna, and N Pugno. Scaling of energy dissipation in crushing and fragmentation: A fractal and statistical analysis based on particle size distribution. *International Journal of Fracture*, 129:131–139, 2004.
- [13] A Cho. Life’s patterns: No need to spell it out? *Science*, 303:782–783, 2004.
- [14] D Cohen. Computer simulation of biological pattern generation processes. *Nature*, 216:246–248, 1967.
- [15] W Colangelo, B Lamont, A Jones, D Ward, and S Bombardieri. The anatomy and chemistry of the colour bands of grasstree stems (*Xanthorrhoea preissii*) used for plant age and fire history determination. *Annals of Botany*, 89:605–612, 2012.
- [16] J Considine and K Brown. Physical aspects of fruit growth - theoretical analysis of distribution of surface growth forces in fruit in relation to cracking and splitting. *Plant Physiology*, 68:371–376, 1980.
- [17] T Courtat, C Gloaguen, and S Douady. Mathematics and morphogenesis of the city: A geometric approach. *Physical Review E*, 83:036106, 2011.

- [18] H Dale, A Runions, D Hobill, and P Prusinkiewicz. Modelling biomechanics of bark patterning in grasstrees. *Annals of Botany*, 114:629–641, 2014.
- [19] RO Erickson. The geometry of phyllotaxis. In *The growth and functioning of leaves*, pages 53–88. Cambridge: University Press, 1983.
- [20] P Federl. Modeling fracture formation on growing surfaces. *Ph.D. thesis*, University of Calgary, 2002.
- [21] P Federl and P Prusinkiewicz. A texture model for cracked surfaces. *Proceedings of the Seventh Western Computer Graphics Symposium, 4-6 March 1996.*, pages Panorama, British Columbia, Canada. 23–29, 1996.
- [22] P Federl and P Prusinkiewicz. Finite element model of fracture formation on growing surfaces. In M. Bubak, G. van Albada, P. Slood and J. Dongarra (Eds.), *Proceedings of ICCS 2004. Lecture Notes in Computer Science 3037 - Part II.*, pages Berlin: Springer. 138–145, 2004.
- [23] DR Fowler, P Prusinkiewicz, and B Johannes. A collision-based model of spiral phyllotaxis. In *ACM SIGGRAPH Computer Graphics*, volume 26, pages 361–368, 1992.
- [24] AM Gill and F Ingwersen. Growth of *Xanthorrhoea australis* R. Br. in relation to fire. *Journal of Applied Ecology*, 13:195–203, 1976.
- [25] NJ Giordano and H Nakanishi. *Computational physics.*, 2nd edn. West Lafayette: Benjamin Cummings, 2005.

- [26] D Gross and T Seelig. *Fracture mechanics with an introduction to micromechanics*. 2nd edn. Heidelberg: Springer, 2011.
- [27] M Hickey and C King. *The Cambridge illustrated glossary of botanical terms*. Cambridge University Press, 2001.
- [28] I Jolliffe. *Principal Component Analysis*,. 2nd edn. Canterbury: Springer, 2012.
- [29] I Kleiner. Evolution of the function concept: A brief survey. *The College Mathematics Journal*, 20:282–300, 1989.
- [30] R Kumar. Pandanas tectorius. Care by herbal <http://carebyherbal.blogspot.ca/search/label/PANDANUS%20TECTORIUS>.
- [31] BB Lamont, R Wittkuhn, and D Korczynskyj. Ecology and ecophysiology of grasstrees. *Australian Journal of Botany*, 52:561–582, 2004.
- [32] TK Lim. Pandanus tectorius. In *Edible medicinal and non-medicinal plants*, pages 136–146. Springer, 2012.
- [33] BB Mandelbrot. *The fractal geometry of nature*. W. H. Freeman, 1983.
- [34] B Margherita and EW Weisstein. Cantor set. In *MathWorld - A Wolfram Web Resource*. <http://mathworld.wolfram.com/CantorSet.html>.
- [35] T Matsuyama and M Matsushita. Fractal morphogenesis by a bacterial cell population. *Critical Reviews in Microbiology*, 19:117–135, 1993.
- [36] M Merlin. Plants and environments of the Marshall Islands: Bob fruit photograph. <http://www.hawaii.edu/cpis/MI/plants/bob.html>.

- [37] National Human Genome Research Institute: National Institutes of Health. An overview of the human genome project: What was the human genome project? <http://www.genome.gov/12011238>.
- [38] N Packard. Lattice models for solidification and aggregation. *First International Symposium for Science on Form*, pages 95–101, 1986.
- [39] M Pauly, M Gross, and LP Kobbelt. Efficient simplification of point-sampled surfaces. *Proceedings of Visualization 02*, pages 163–170, 2002.
- [40] BE Pons. Generalized self-contacting symmetric fractal trees. *Symmetry: Culture and Science*, 21:333–351, 2013.
- [41] P Prusinkiewicz and P Barbier de Reuille. Constraints of space in plant development. *Journal of Experimental Botany*, 61:2117–2129, 2010.
- [42] P Prusinkiewicz and A Lindenmayer. *The algorithmic beauty of plants*. New York: Springer-Verlag, 1990.
- [43] P Prusinkiewicz, L Mundermann, R Karwowski, and B Lane. The use of positional information in the modeling of plants. *Proceedings of SIGGRAPH 2001*. New York: ACM SIGGRAPH, pages 289–300, 2001.
- [44] JN Ridley. Ideal phyllotaxis on general surfaces of revolution. *Mathematical Biosciences*, 79:1–24, 1986.
- [45] P Rudall. Lateral meristems and trunk thickening growth in monocotyledons. *Botanical Review*, 57:150–163, 1991.

- [46] E Sharon, M Marder, and HL Swinney. Leaves, flowers and garbage bags: Making waves. *American Scientist*, 92:254–261, 2004.
- [47] E Sharon, B Roman, M Marder, GS Shin, and HL Swinney. Buckling cascades in free sheets. *Nature*, 419:579, 2002.
- [48] K Shinozaki, K Yoda, K Hozumi, and T Kira. A quantitative analysis of plant form - the pipe model theory, parts I and II. Basic analysis and further evidence of the theory and its application in forest ecology. *Japanese Journal of Ecology*, 14:97–104, 133–139, 1964.
- [49] AT Skjeltorp and P Meakin. Fracture in microsphere monolayers studied by experiment and computer simulation. *Nature*, 335(6189):424–426, 1988.
- [50] NJA Sloane and S Plouffe. OEIS Foundation Inc. The on-line encyclopedia of integer sequences. Sequence A006519 - Highest power of 2 dividing n. <http://oeis.org/A006519>, 1991.
- [51] IA Staff. A study of the apex and growth patterns in the shoot of *Xanthorrhoea media* R. Br. *Phytomorphology*, 18:153–165, 1968.
- [52] R Tan. Mengkuang or Seashore pandanus (*Pandanus tectorius*). flickr: <https://flic.kr/p/bzSMYo>.
- [53] LAJ Thomson, L Englberger, L Guarino, RR Thaman, and C Elevitch. *Pandanus tectorius* (pandanus). In *Species profiles for Pacific island agroforestry, ver. 1.1*. <http://www.traditionaltree.org>. 2006.

- [54] H Trochet. A history of fractal geometry. In MacTutor History of Mathematics <http://www-groups.dcs.st-and.ac.uk/~history/HistTopics/fractals.html>, 2012.
- [55] S Ulam. On some mathematical problems connected with patterns of growth of figures. In *American Mathematical Society Proceedings of Symposia in Applied Mathematics*, 14:215–224, 1962.
- [56] G Van Iterson. *Mathematische und mikroskopisch-anatomische Studien über Blattstellungen*. Gustav Fischer: Jena, 1987.
- [57] EW Weisstein. Koch snowflake. In *MathWorld - A Wolfram Web Resource*. <http://mathworld.wolfram.com/KochSnowflake.html>.
- [58] EW Weisstein. Sierpinski sieve. In *MathWorld - A Wolfram Web Resource*. <http://mathworld.wolfram.com/SierpinskiSieve.html>.
- [59] L Wolpert, R Beddington, TM Jessell, P Lawrence, EM Meyerowitz, and J Smith. *Principles of development*. New York: Oxford University Press, second edition, 2002.

Appendix A

Ridley's model of phyllotactic on the grasstree dome

The dome-like top to the grasstree was modeled by A. Runions and attached to the cylindrical trunk of the grasstree model such that the phyllotactic patterns matched. This section is presented as an appendix as it is primarily visual (i.e. not affecting the patterns produced by the model) and was not created by myself.

The dome is modeled as a surface of revolution, obtained by rotating a graphically defined profile curve around the tree axis (Fig.A.1). At its base, the dome is connected to the cylindrical trunk. All leaves were positioned using the Ridley [44] model of phyllotaxis, previously applied to computational modeling by Prusinkiewicz et al [43]. Ridley's model packs organs on the supporting surface by assuming a fixed divergence angle and by displacing the organs vertically according to the area that they occupy. In this implementation, Ridley's model operates dynamically, with new leaves inserted at the tip of the apical dome as the space becomes available for them. This increase is a joint effect of primary and secondary growth.

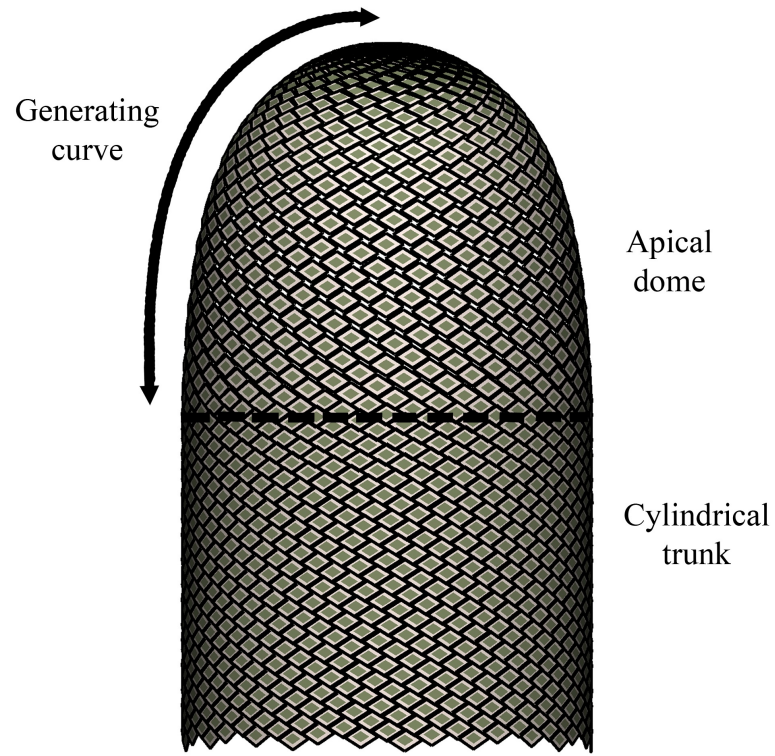


Figure A.1: Geometry of the tree trunk and a sample distribution of leaf bases generated using Ridley's [44] model. For clarity, leaf bases are larger and less numerous than in the actual grass tree and the full model. The profile of the apical dome is defined by a generating curve. The dome is smoothly connected to the cylindrical trunk. The division between these two regions is marked by the dotted line.

Appendix B

An exploration of the emergence of form and fractal structure in simple branching models

B.1 Introduction

This appendix presents a preliminary analysis of how simple, uniformly branching structures can emergently develop structure and fractal form through collisions between branches. Fractals display self-similarity such that the same structure is repeated across different scales of the object. The term fractal was introduced by Benoit Mandelbrot and made popular in his renowned book, “The Fractal Geometry of Nature” [33].

The trail that lead Mandelbrot to coining the term fractal started in 1872 with the discovery by Weierstrass of functions that are continuous but nowhere-differentiable [29]. Weierstrass showed that certain analytic functions can have no tangents [54] and when plotted, these functions lack smoothness and appear very irregular. This was a surprising find that went against classical mathematics and ultimately became the inspiration for the early fractal founders.

Cantor devised a structure that is composed of a line segment with the middle third removed from the remaining line segments, see Fig. B.1 A. As the process continues, smaller and smaller line segments are produced eventually leading to an infinite number of points. The strange property of this set is that the original line

segment also contained an infinite number of points, and so, by removing a third each time, the set is somehow still left with an infinite number of points [34]. This broken line structure became one of the first self-similar and early fractal forms called the Cantor set. Another early pioneer was von Koch who in 1904 published what became known as the Koch curve, Fig. B.1 B. This curve is created from an equilateral triangle with the middle third of each edge replaced with another equilateral triangle [57]. This was one of the first closed curves to have the strange property of infinite length but finite area.

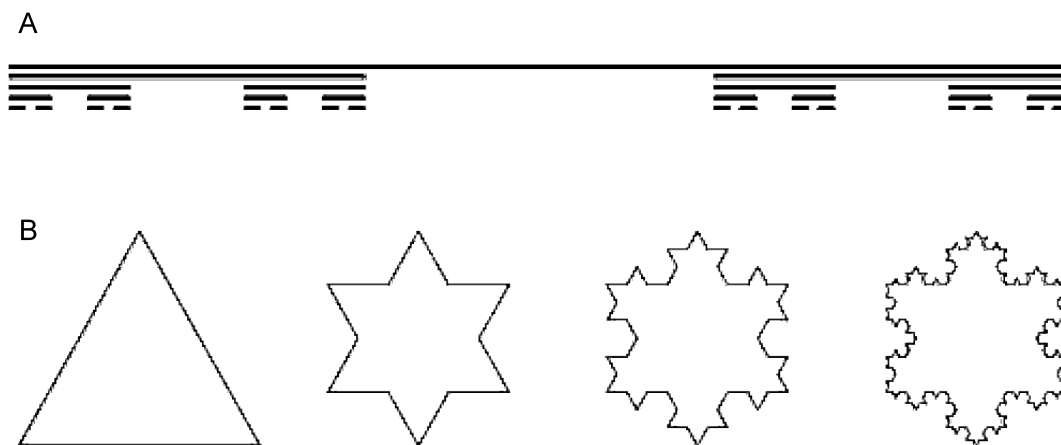


Figure B.1: The Cantor set (A) and Koch curve (B). Images from WolframMathWorld [34] and [57], respectively.

The Sierpinski gasket, another early fractal formation and important to this appendix, was described in 1915 by Waclaw Sierpinski [58]. The gasket can be formed by starting with an equilateral triangle and recursively removing a middle equilateral triangle from each of the remaining sections, Fig. B.2.

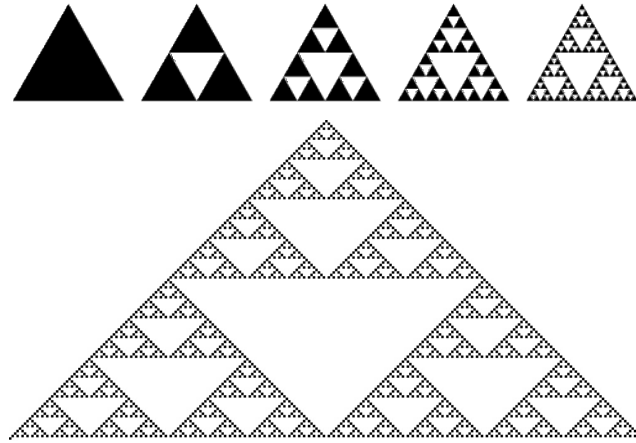


Figure B.2: Sierpinski gasket. Images from WolframMathWorld [58].

These structures with sometimes non-integer dimension and ever repeating copies of themselves interested Mandelbrot and lead him to realize that much of nature is composed of these structures, “Clouds are not spheres, mountains are not cones, coastlines are not circles, and bark is not smooth, nor does lightning travel in a straight line” [33].

An analysis of how collisions between objects due to limited space can produce form and fractal character in simple models of structural growth is presented. Collisions are an inherent part of the space we live in, no two classical objects can occupy the same space at the same time. Although rudimentary, this inherent rule of space can be a powerful tool to shape structures into complex forms when the rules for growth are simple and uniform.

Ulam was the first to study colliding branching structures. He introduced a branching structure with branches at 90° to each other, Fig B.3 and named this structure the “Maltese crosses”. The resulting formation is an emergent self-similar

fractal pattern that arises through the collisions between branches. Cohen was also one of the first who studied branching structures at the time it was possible to use computers to create simulations [14]. Cohen considered the external environment as well by imposing a density field, from the neighboring parts of the structure, on the direction of the branches and he also used a limiting density above which no growth can occur.

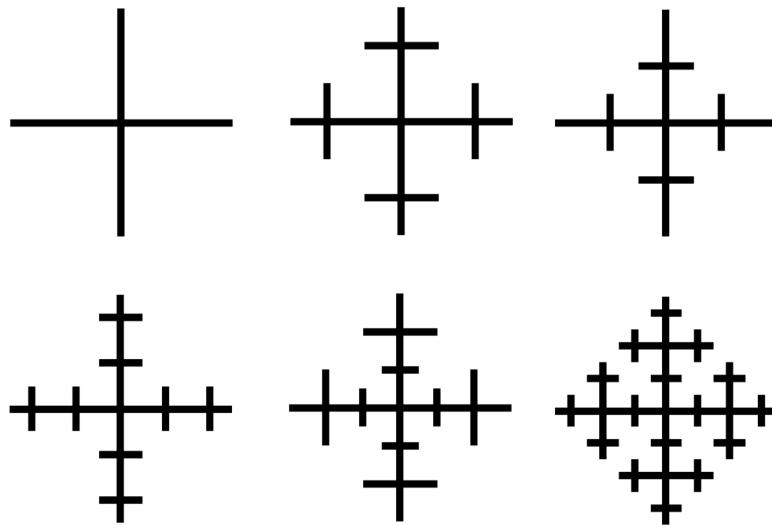


Figure B.3: Progression of the Ulam Maltese crosses from top left to bottom right.

B.2 Model

The basic branching model considered here consists of a 2D planar branching structure that grows iteratively by extending upon previous branches in all possible direction except those that result in an intersection, or collision, with another branch. There rule for growth are:

1. Branches grow iteratively by extending upon branch tips by a fixed length by either elongating existing branches or creating new side branches.
2. Possible branching angles for an n-branch system are $\frac{2\pi}{n}$, where n is the number of branches. If the number of branches is 2, the angle between branches is $< \pi$ (an angle of π would result in a straight line structure with the structure overlapping itself). Angles are defined relative to axes in the plane as opposed to relative to the branches.
3. Branches grow in all n directions. If a branch segment (line) intersects another branch segment, one (or both) of the branch segments are removed. Specifics on how collision detection is determined and the properties of the space around branches that were involved in collisions are discussed in the next sections.

Each figure starts with an initial n branches for which other branches can grow upon, the rules are illustrated in Fig B.4.

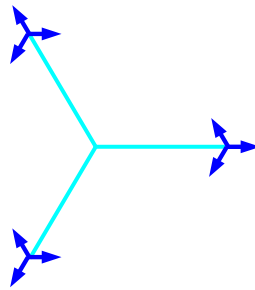


Figure B.4: 3-branch system with the initial 3 branches (light blue) that each attempt to grow 3 more branches (dark blue arrows) at the next iteration.

The branch tips are stored as points in an array. The iteration number that each branch was initiated at, or the age of the branch, is also stored, along with the

corresponding branch tip that it grew off of so that the structure could be visualized. When branches can not fit in the space, a collision is detected.

B.3 Collision detection

Collision detection was determined between branch segments (line segments). Each branch segment is defined by the branch tip (point) of that branch and the branch tip of the branch from which it grew off (also a point), and a line or branch segment that is drawn between the two. Each new branch segment was tested to see if an overlap with an existing branch segment or a new branch segment, also created during that iteration, occurred. If an intersection did occur, a collision was detected and that new branch segment was removed from the simulation.

To test for an intersection between branch segments, an intersection point of the two lines was determined for nonparallel lines. The intersection point was then tested to see if it was within the boundaries of both line segments, if it was a collision was detected. For parallel lines, the lines were first tested to see if the line segments were along the same line, if so the end points of the line segments were then checked to see if an overlap occurred and therefore a collision occurred.

The first iteration of a 2-branch system is shown in Fig. B.5. The left image in (A) shows the initial configuration for a 2-branch system. The next iteration shown on the right shows how each branch grows 2 branches, in the directions $\theta = 0^\circ$ and $\theta = 60^\circ$ for this simulation. The branches which branch off of each main branch axis, in the direction of the other branch, collide with each other. Both branch tips try to occupy the same space. This type of collision is relieved in (B) where the secondary

branches that run off of the main axes are removed.

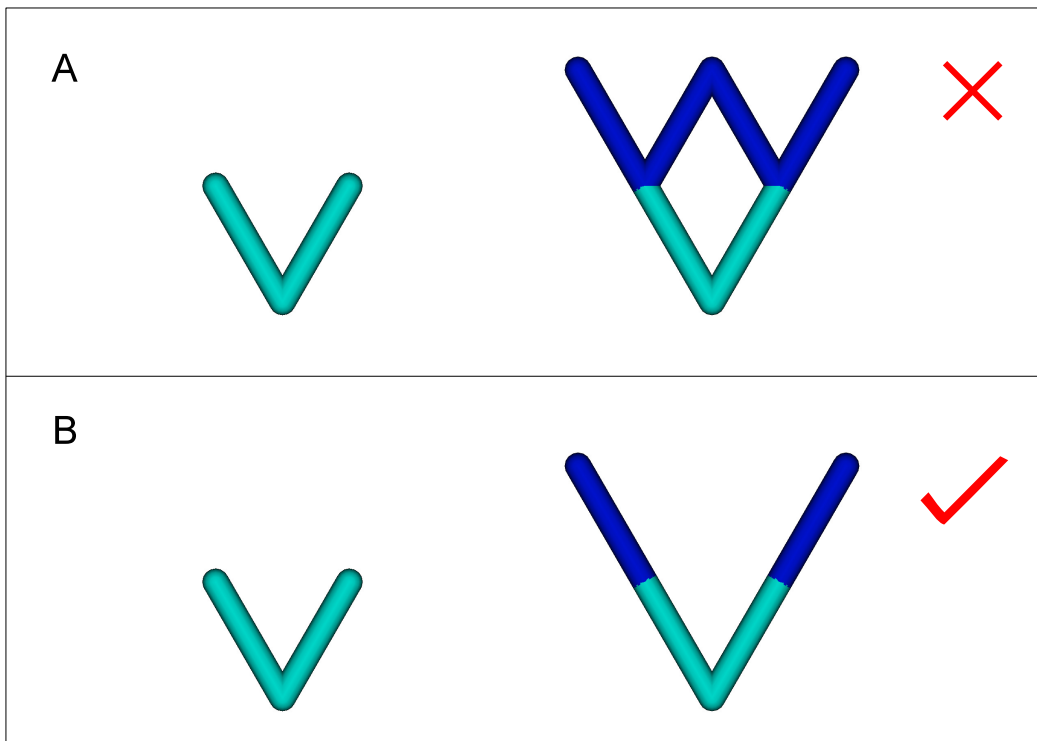


Figure B.5: First and second iteration of the 2-branch system showing how branches collide (A) and then are removed leaving only the branches that have enough space (B).

The continuation of this process is shown in Fig. B.6 where branches extend upon previous branches and those that intersect other branch segments are removed.

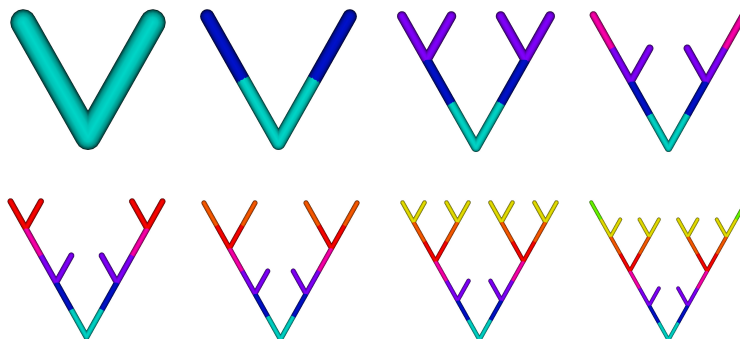


Figure B.6: 2-branch system showing different iterations of growth (from top left to the bottom right).

As this process continues, the 2-branch figure starts to look more self-similar and begins to produce a Sierpinski gasket, Fig. B.7.

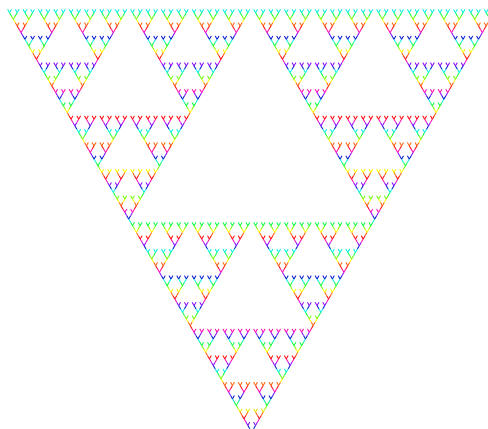


Figure B.7: Larger number of iterations for the 2-branch system.

This Sierpinski gasket formation in the 2-branch system does not seem to be dependent on the angle, Fig. B.8 shows the same model with angles 120° , 90° and

45°.

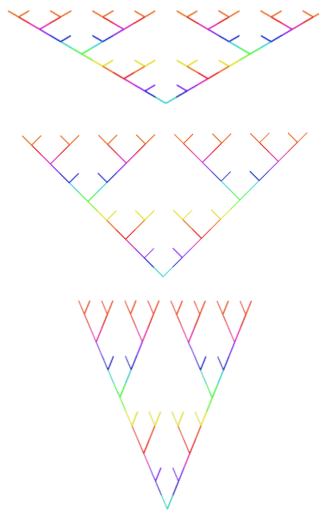


Figure B.8: 2-branch system with 3 different angle. Top angle is 120° , middle image is 90° and bottom image is 45° .

This model can be extended to analyze structures with a larger number of branches. Fig. B.9 shows the initial 8 iterations of a 3-branch system and Fig. B.10 shows the 3-branch system with a larger number of iterations.

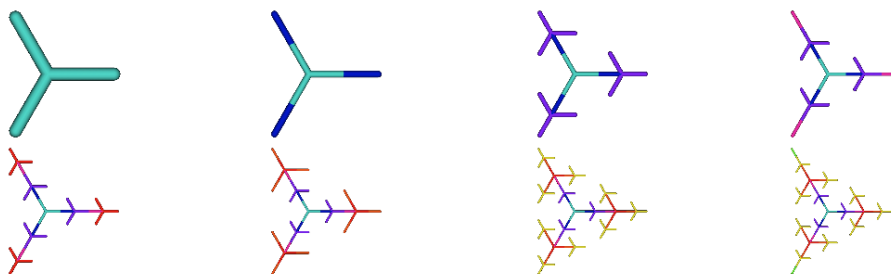


Figure B.9: 3-branch system showing different iterations of growth (from top left to the bottom right).

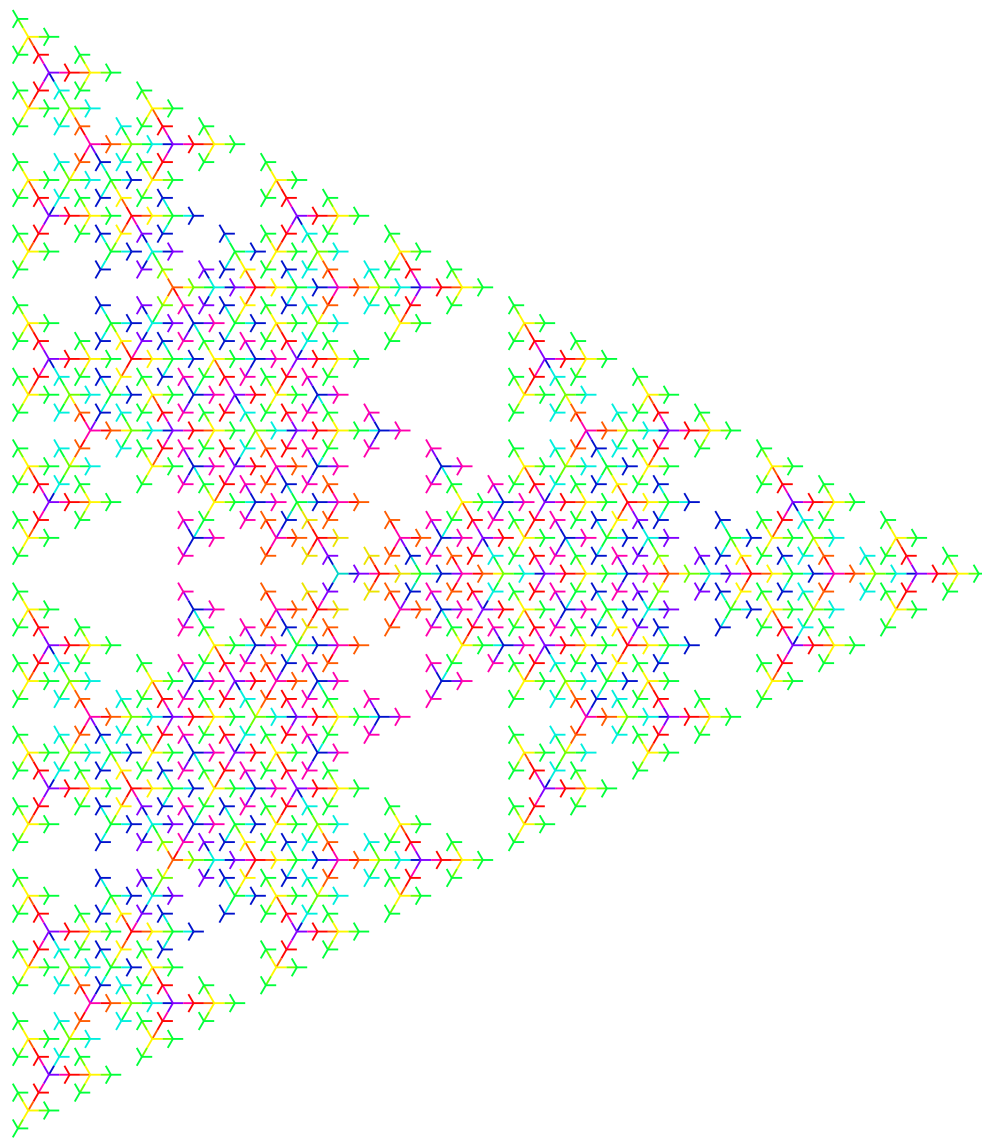


Figure B.10: Larger number of iterations of the 3-branch system.

The 3-branch system appears to be strictly self-similar, Fig. B.11 shows how the 3-branch structure is repeated throughout the figure on different scales.

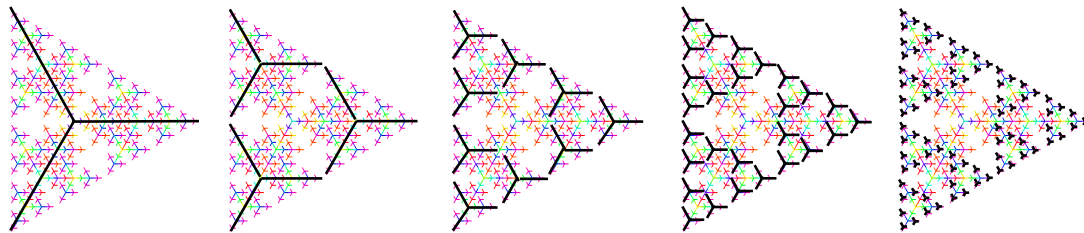


Figure B.11: 3-branch structure repeated on different scales.

The 4-branch system produces a similar pattern to the Ulam pattern shown in Fig. B.3 but an alternating pattern on the secondary branches is produced, Fig. B.12.

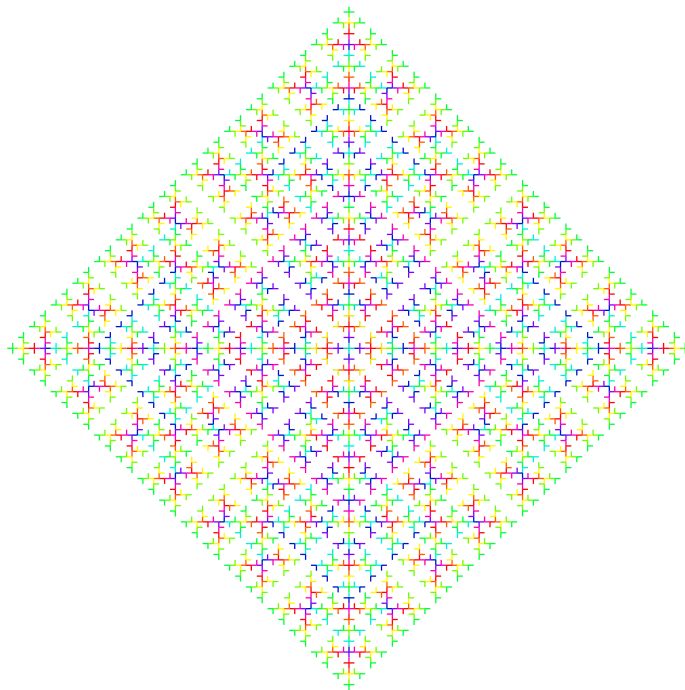


Figure B.12: Large number of iterations of the 4-branch system.

Fig. B.13 shows the 5-branch system which is able to fit in a lot of branches in

the empty spots through creating zigzag segments.

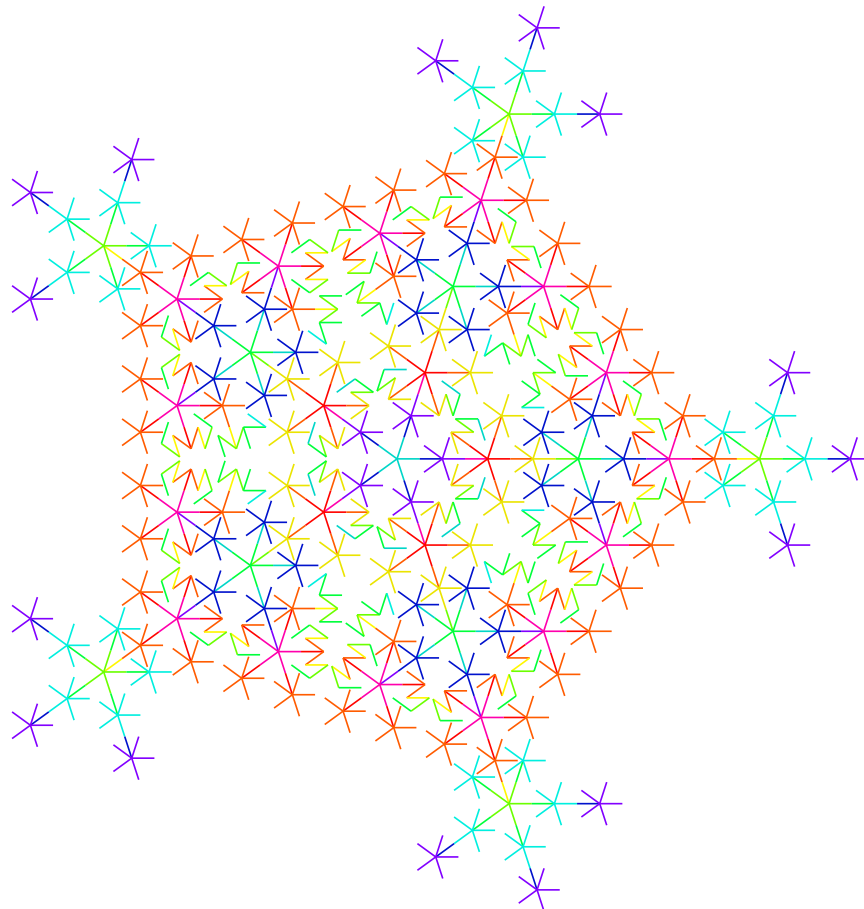


Figure B.13: 5-branch system with precise collision detection produces many interior branches.

Figures with more than 5 branches cannot progress past the initial configuration. Fig. B.14 shows where collisions occur on the n -main branches which prohibits the main branches from progressing any further. The 6-branch system has a collision right at the tips of the initial 6 branches, which prevent them from growing forwards.

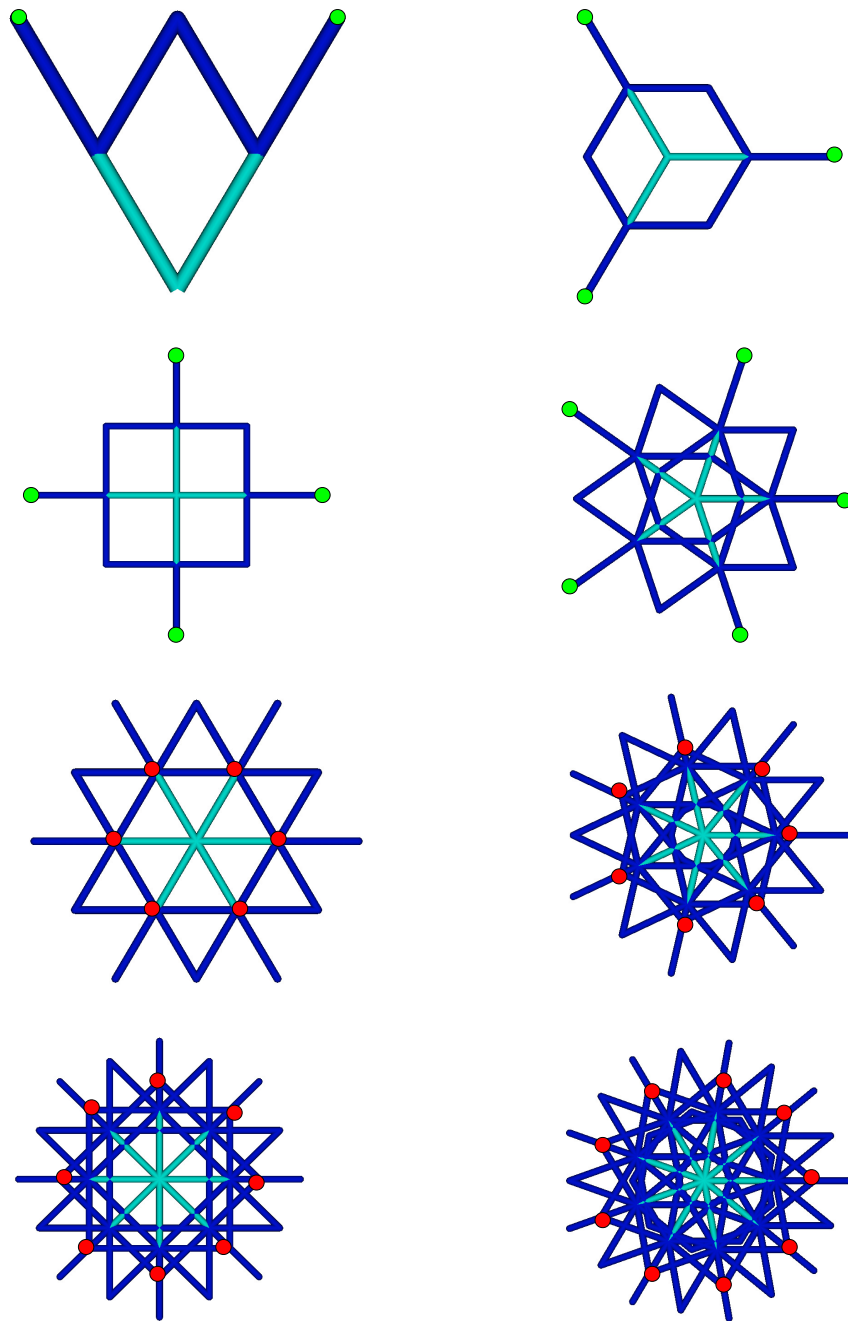


Figure B.14: 2-9-branch systems with collision detection between the branch segments. Green dots indicate main branches which can continue to grow and are not involved in a collision, red dots indicate where collisions on the main branches occur which prevent them from growing any further.

B.3.1 Continuous approximation to collision detection

To produce branching structure with more than 5 branches, a more continuous approach to collision detection was implemented. Branch intersections (line or point intersections) were resolved depending on which branch would have reached the intersection point first if it were a continuous growth model. Fig. B.15 shows two branches at an angle 40° to each other (light blue). The next iteration (dark blue) a secondary branch from the main branch at 0° intersects the branch moving in the direction of the other main branch at 40° (red circle). This intersection occurs at the tip of the secondary branch and close to half way along the other branch segment. If this were a continuous growth model, the branch in the direction of the main branch at 40° would have reached the intersection point before the other secondary branch. Therefore the branch in the direction of the main branch survives and the other is removed as shown on the right of Fig. B.15.

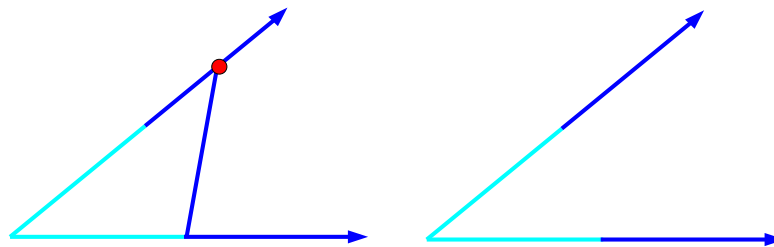


Figure B.15: Continuous approximation to collision detection. Branches which would have reached the intersection point first, stay and the others are removed.

To resolve collisions, branches which intersected branches from a previous iteration were removed, Fig. B.16 A. Branches of the same iteration that intersected

were tested against each other to determine which branch could stay and which were removed. This was simulated by determining which branch tip was the furthest from the intersection point, such that it would have reached that intersection point first. The branch segment that was the furthest survived and all other branches intersecting with it were removed, Fig. B.16 B. If the longest distance from the base of the branch is the same for two branches, both branches were removed, Fig. B.16 C. Fig. B.17 shows 2-9-branch systems with the continuous method for collision detection.

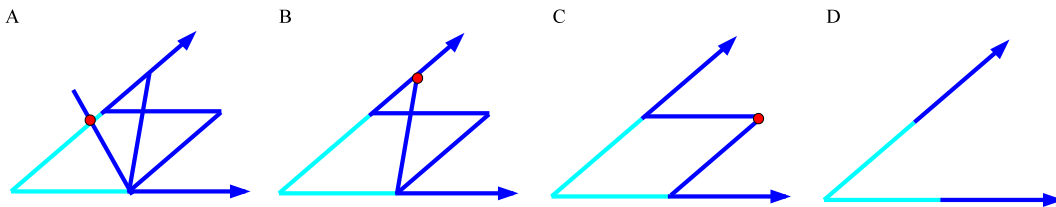


Figure B.16: Rules for continuous collisions. Branches intersecting other branches of a previous iteration are removed (A), branches which intersect other branches at a larger distance from the base than the other branches is removed (B) and branches that intersect other branches at the same point are removed (C).

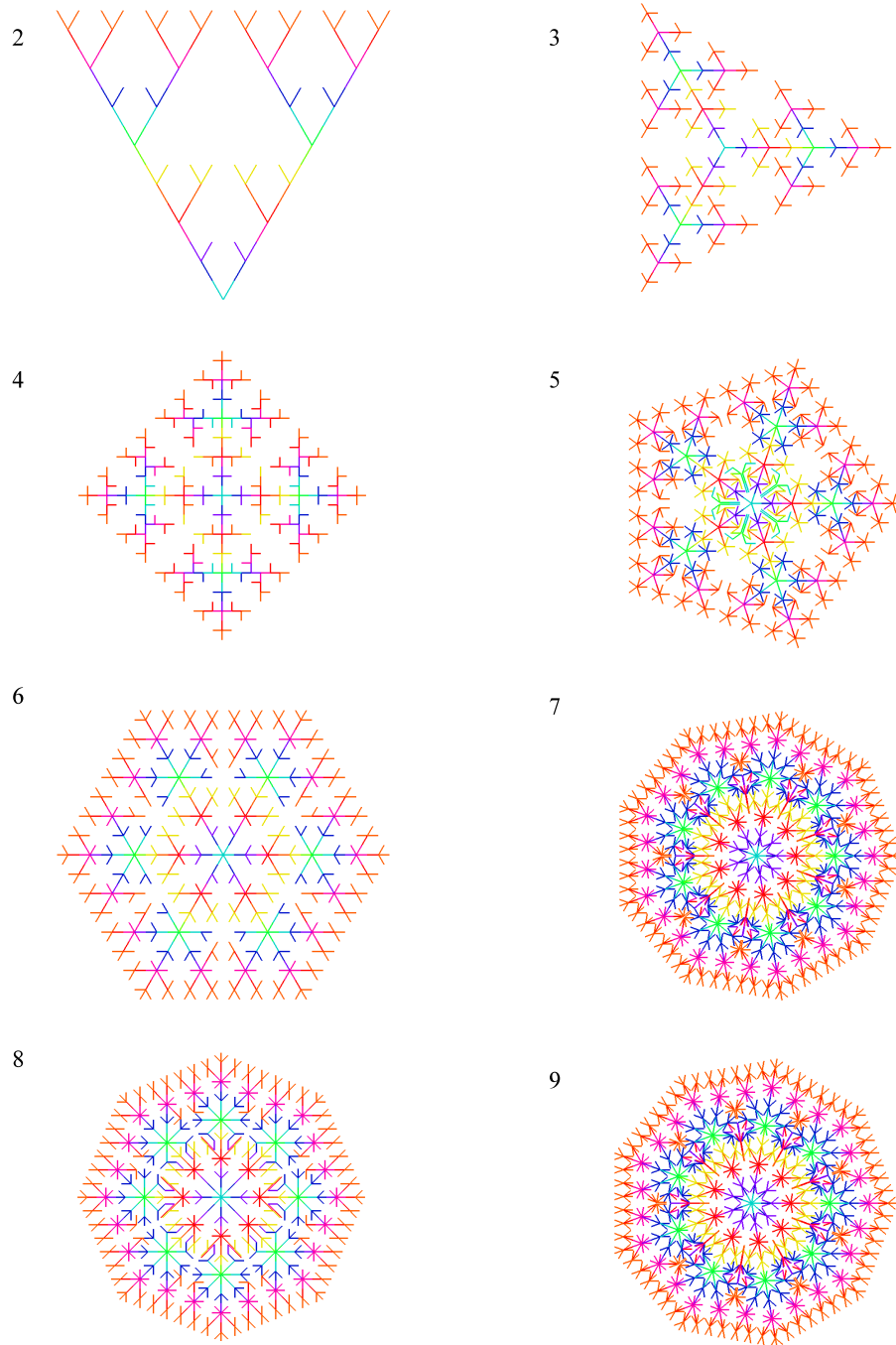


Figure B.17: Different branching systems using a continuous approximation to collision detection.

The branches which were involved in collisions and removed from the simulation are rewritten over in the array of branch tips and nonexistent in the next iterations. This allows for other branches to move into those spaces if they are available. The branch tips which have branches removed from them are considered to have “dead buds”, because once they are removed they never grow again. The next section analyzes what happens when branch tips which are involved in collisions are not rewritten over but are still kept in the array of branch tips but are labelled as “dormant buds”.

B.4 Dormant buds

So far the types of branch tips that have been looked at have been of a dead type, meaning once the branch is in a collision, it never tries to grow into that space again. This section illustrates another type of branch tip, or bud type, dormant buds. Dormant bud branch tips are always trying to grow into the space around them, even if they have been removed, and thus no other branches can move into that space.

Dormant buds were handled in a similar way to dead buds except that the array of branch tips was not rewritten over when branches were removed from the simulation due to collisions. Keeping track of all of the generated branches meant that new branches were not able to move into the space that a previous branch tried to grow into because they would collide with the dormant buds constantly creating the same branches. Branches that were involved in collisions were marked as dormant so they were not visualized in the simulation, 2-9-branch structures are shown in Fig. B.18.

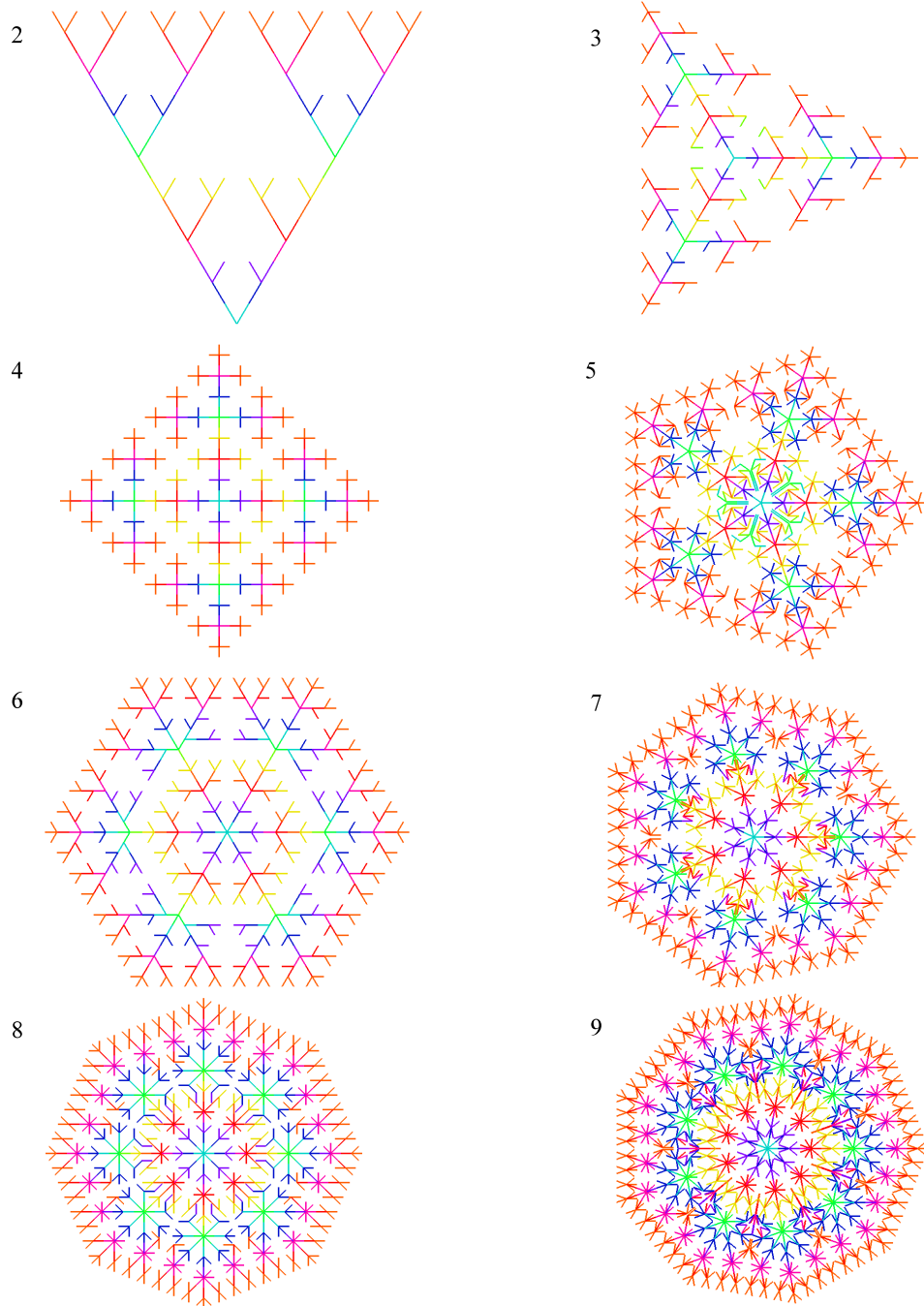


Figure B.18: Different branching systems with dormant buds

There are differences in the 3, 4, 6 and 7-branch structures for dead vs. dormant buds, Fig. B.19 red lines, whereas the 2, 5, 8 and 9-branch structures are the same for the different bud types (at least up to the generation shown), Fig. B.19 green lines. The 3-branch system changes from an opposite-type branching system with dead buds where it exhibits self-similarity to an alternating one when the buds are dormant, Fig. B.20 top. On the other hand, the 4-branch system changes from an alternating branching pattern with dead buds to an opposite-type branching system where it exhibits self-similarity when the buds are dormant, Fig. B.20 bottom. The 4-branch system with dormant buds produces the Ulam pattern.

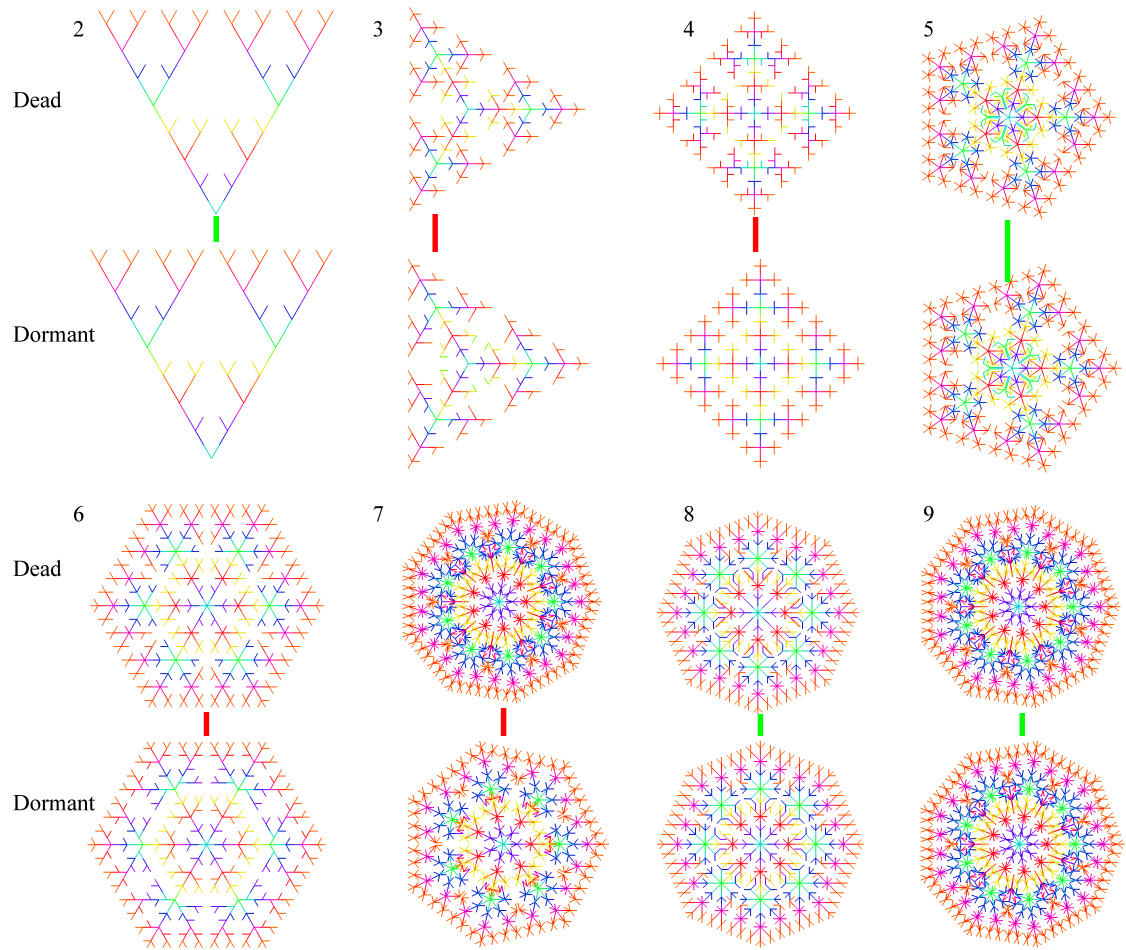


Figure B.19: Branching systems with dead and dormant buds. Green lines indicated that the resulting pattern is the same (up to the iteration shown) and red lines indicate that the patterns from different bud types are different.

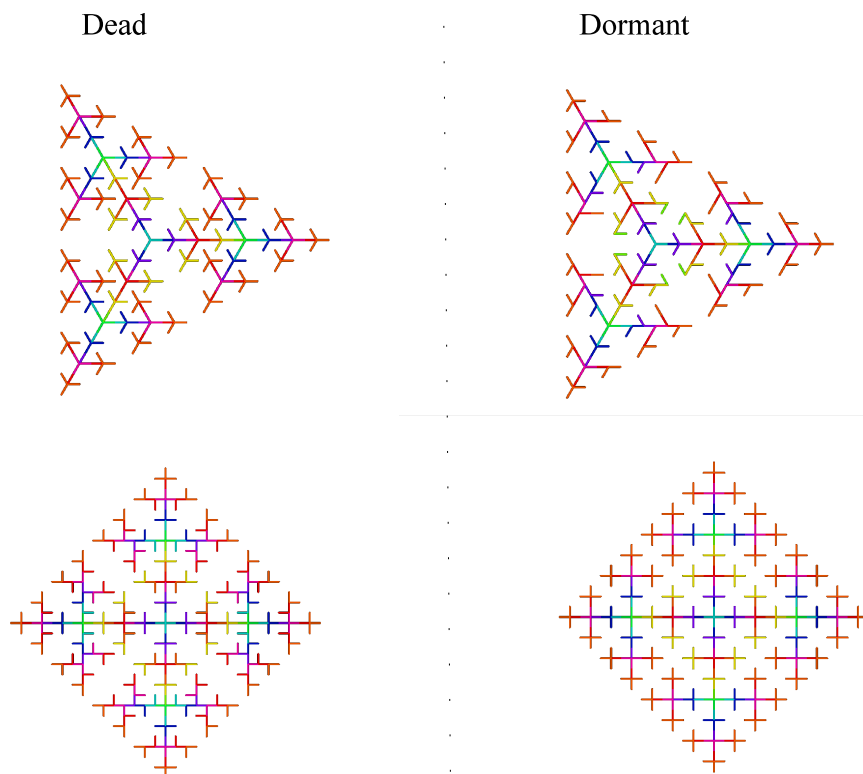


Figure B.20: Dead and dormant bud types for the 3 and 4-branch systems.

B.5 Self-similarity

The 2, 3 and 4-branch systems appear to be able to produce self-similar structures. The 2-branch system, for both dead and dormant buds, produces the Sierpinski gasket and is self-similar. The 3-branch system is self-similar when the buds are dead and the 4-branch system is self-similar when the buds are dormant and produces Ulam Maltese crosses.

One possible reason for the 3 and 4-branch systems exhibiting self-similarity

with different types of buds is because they have different symmetries. The 3-branch system does not have mirror symmetry across the y -axis (90° line) and after the first iteration it becomes a 4-branch system whereas the 4-branch system remains a 4-branch system and has mirror symmetry across both the x and y axes. Fig. B.21 illustrates the first few iterations of one of the main branches of the 3 and 4-branch systems to show how self-similarity is affected by the bud type. Black dots denote points that are occupied by other branches trying to move into those spots (outlined in black dashed lines). In the 3-branch case, the dormant buds take up the space that the left tertiary branch would occupy (red dashed line) but not on the right side, which eventually leads to the establishment of an alternating branching pattern on the secondary branches. In the 4-branch case, the dead buds allow for an early branch on the left tertiary branch but not on the right side where the main branch also produces a secondary branch that collides with it. This premature branching leads to an alternating pattern on the secondary branches.

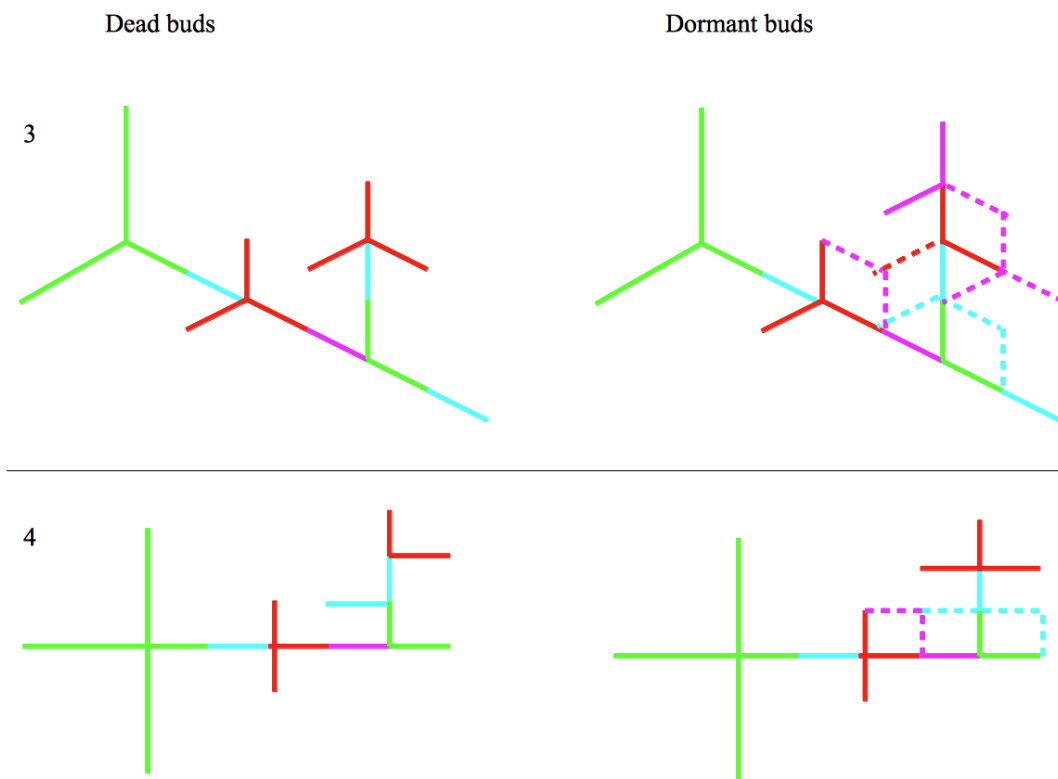


Figure B.21: Dead and dormant buds for 3 and 4-branch systems. Alternating branching patterns occur on the 3-branch system with dormant buds and the 4-branch system with dead buds. Colors indicate different iterations, dashed lines represent previous branches that were removed due to a collision but still occupy that space.

B.6 Length of longest branch

Commonalities between the different branching structures were determined in the hopes of finding general characteristics between the models of different branching numbers and bud types. Finding similarities between these different systems will

show what the impact of the basic model (symmetric growth by extending upon branch tips and collisions between branches that intersect), as opposed to specific features (i.e. number of branches), is on form. To determine common patterns among the different branching systems, a measurement that can be done is to look at the length of the longest secondary branch that comes off of the primary branches (the original n branches). Every one of the 2D systems analyzed has a sequence for the length of the secondary branches starting at the first iteration of: 0, 1, 0, 3, 0, 1, 0, 7, 0, 1, 0, 3, 0, 1, 0, ... as shown in Fig. B.22.

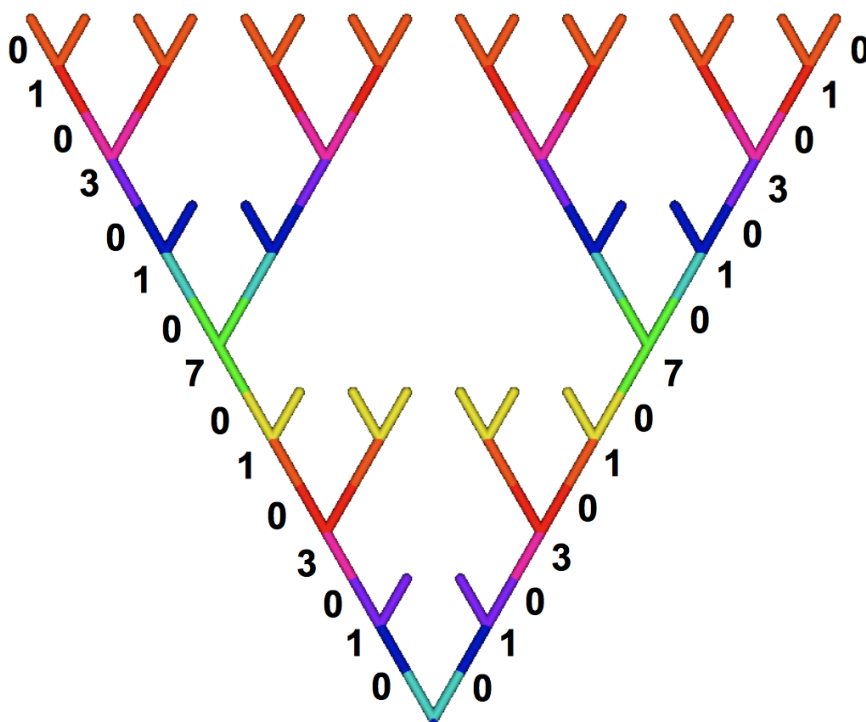


Figure B.22: 2-branch system showing the length of the secondary branches.

Additional iterations produces the sequence:

$$\begin{aligned}
&0, \mathbf{1}, 0, \mathbf{3}, 0, 1, 0, \mathbf{7}, 0, 1, 0, 3, 0, 1, 0, \mathbf{15}, 0, 1, 0, 3, 0, 1, 0, 7, 0, 1, 0, 3, 0, 1, 0, \mathbf{31}, 0, 1, \\
&0, 3, 0, 1, 0, 7, 0, 1, 0, 3, 0, 1, 0,
\end{aligned}
\tag{B.1}$$

where the longest new branch is bolded. Adding 1 to each number in the sequence produces, 1, **2**, 1, **4**, 1, 2, 1, **8**, 1, 2, 1, 4, 1, 2, 1, **16**, ...

which is a list of the powers of 2,

$$2^0, 2^1, 2^0, 2^2, 2^0, 2^1, 2^0, 2^3, 2^0, 2^1, 2^0, 2^2, 2^0, 2^1, 2^0, 2^4, \dots$$

This sequence is the “highest power of 2 dividing n” (Sloane’s A006519 [50]). More analysis into this phrase *highest power of 2 dividing n* is presented later in the chapter.

B.7 Underlying Sierpinski gasket pattern

Each of the 2D figures (for both dead and dormant type buds) have an underlying Sierpinski pattern. The sequence of the length of the secondary branches (seq. B.1) is part of the Sierpinski pattern as shown in Fig. B.22 and the higher order branches of the Sierpinski pattern are also a part of all the figures, see Fig. B.23 for an example. Brummit et al. has noted that there exists an embedded Sierpinski pattern in Ulam’s crosses [10] and Pons has noted that there are “Sierpinski gasket trees (symmetric trees with b equally-spaced branches per node)” [40], where b would be the number of branches, but Pons is referring to branching structures with decreasing branch length such that all branches fit without intersection and therefore no collisions.

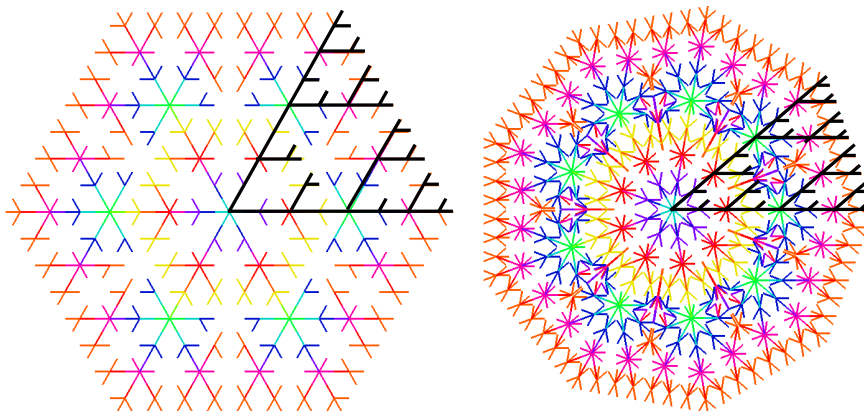


Figure B.23: 6-branch and 9-branch system showing an underlying Sierpinski gasket.

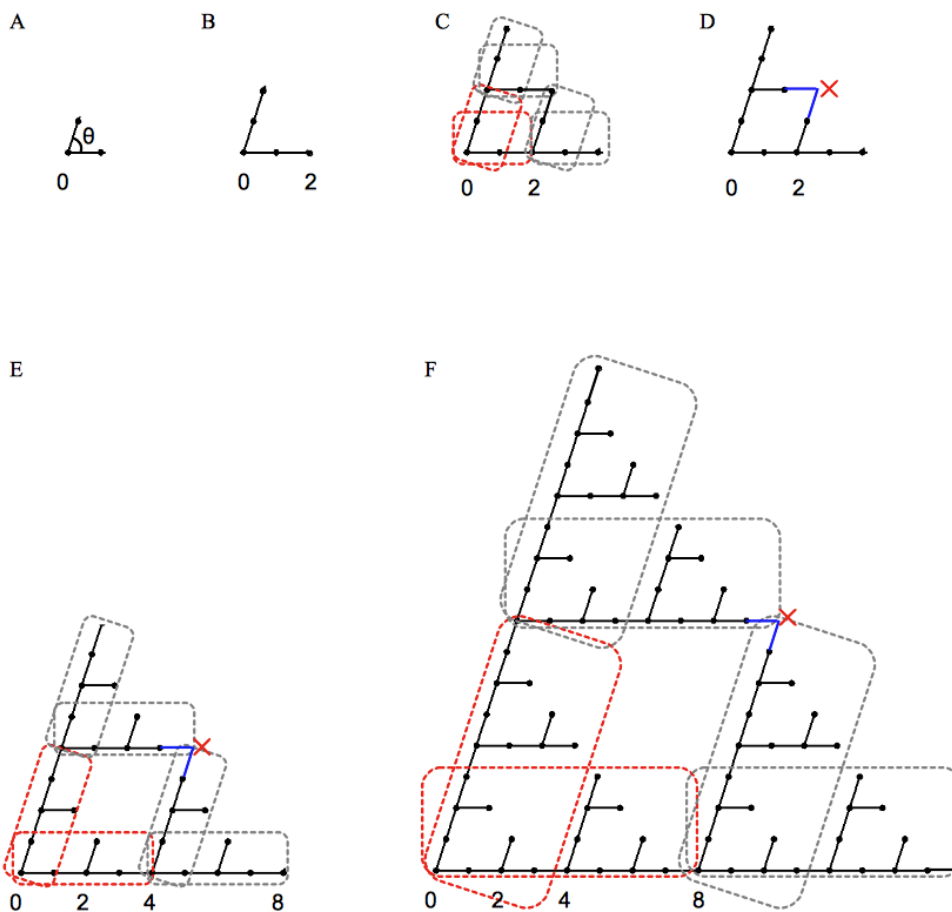
It seems as though this model of growth will always include a Sierpinski gasket between any two main branches of the system and the rest of the branches fill empty spaces around these Sierpinski gasket branches. A sketch of a proof of this concept is illustrated in the next section.

B.8 Steps towards a proof by induction

Steps to create a Sierpinski gasket:

- 1) Start with two branches of unit length at an angle θ from each other (A).
- 2) Each branch adds one branch in the same direction, also of unit length (B).
- 3) The entire structure is repeated on both main branches (C).
- 4) The last branch segment of the secondary branch (in the direction of the other main branch) produced at the beginning of step (3) is removed (D) (blue).
- 5) Repeat steps (3) and (4) infinitely many times.

The entire structure is repeated on both main branches every time the main branches reach a length of 2^n , making the branches a length of 2^{n+1} . The last branch segment of the secondary branch produced at length 2^n is removed. (E) and (F) show these steps when the structure has a length of 4 and 8 respectively.

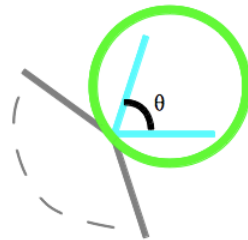


Theorem: n -branch structure with angles $\theta = 2\pi/n$ for $n > 2$ and $\theta < \pi$ for $n = 2$ that grow iteratively by:

- extending upon existing branches by fixed length units in all possible branching angle directions
- branches which intersect a branch from a previous iteration are removed
- branches which intersect branches of the same iteration are not removed if the intersection point is the shortest distance from the base of the branch segment compared to all other branches in the intersection while all other intersecting branch segments are removed. If the shortest distance between the base of the branch and the intersection point is the same for two or more branch segments, all branch segments are removed.

will always produce an underlying Sierpinski gasket formation.

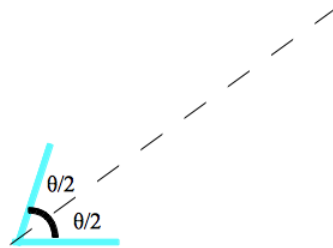
Initial conditions
Iteration #0



n -branch system with angles $2\pi/n$ for $n > 2$ or $\theta < \pi$ for $n = 2$

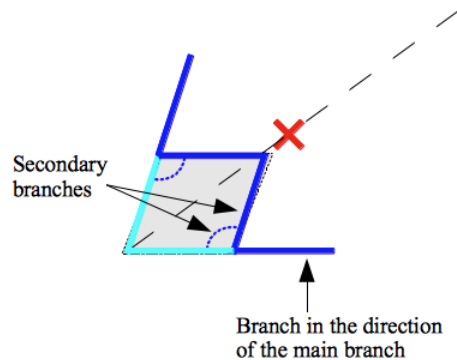
The area between all pairs of branches must behave the same due to symmetry. Only one section between two branches is analyzed.

Iteration #0



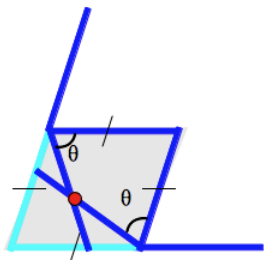
The two main branches impose a constraint of $\theta/2$ on each other for which the other branch formation cannot pass due to symmetry.

Iteration #1



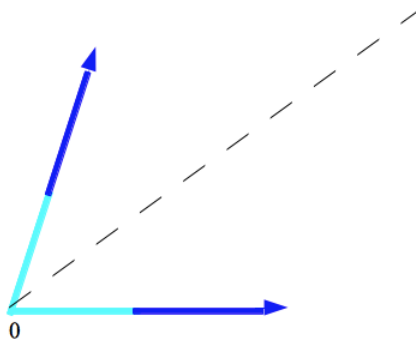
Secondary branches in the direction of the other main branch intersect each other on the line $\theta/2$ in a rhombus formation (grey region) and are removed. Other possible secondary branches are denoted by dashed arcs.

Iteration #1



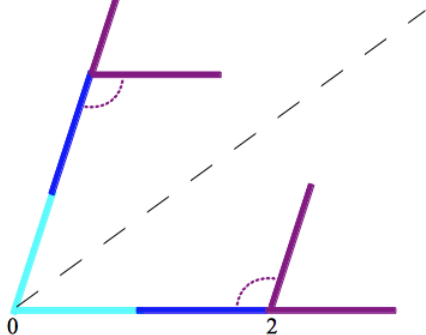
Interior secondary branches intersect the interior secondary branch from the other main branch. The intersection point (red circle) will be the same distance from the base of both branches so both branches will be removed.

Iteration #1



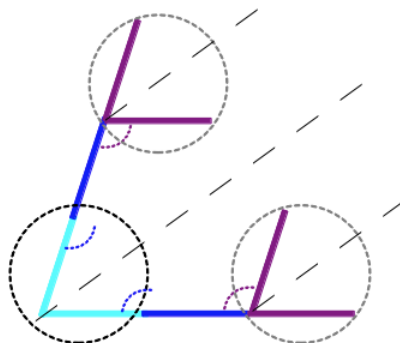
The only surviving branches immediately following a branch junction are in the direction of the main branches.

Iteration #2



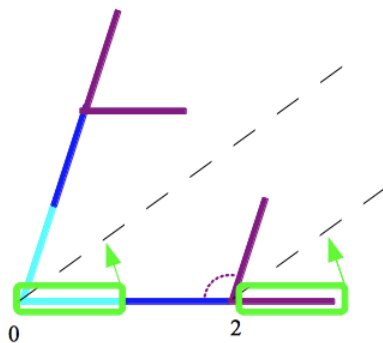
After a branch with no secondary branches is created, a new branch junction can be formed as it fits within the original constraint $\theta/2$.

Iteration #2



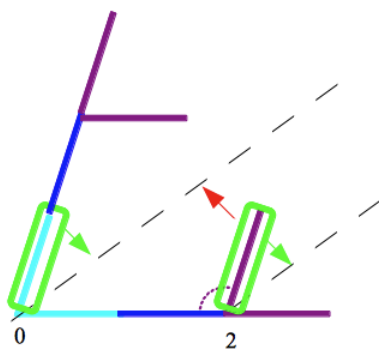
The new branch junctions are similar to the initial branch junction.

Iteration #2



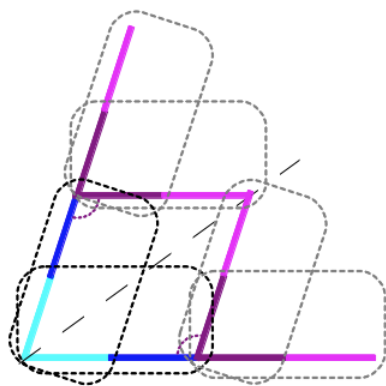
The branch in the direction of the main branch has the same constraints on growth (green arrows) as the initial branch junction (green boxes) and therefore will grow in the same way.

Iteration #2



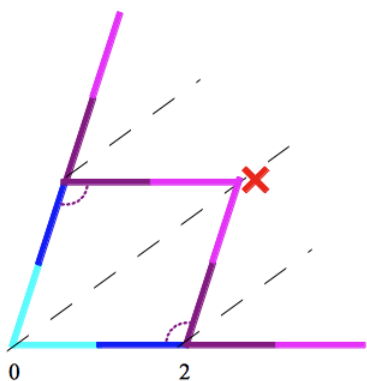
The secondary branch has the same constraint on growth (green arrows) as the initial branch junction in the direction of the other branch (green boxes) with an additional constraint (red arrow) from the initial branch junction that will prevent the branch from growing to a length \geq distance from the original branch junction.

Iteration #3



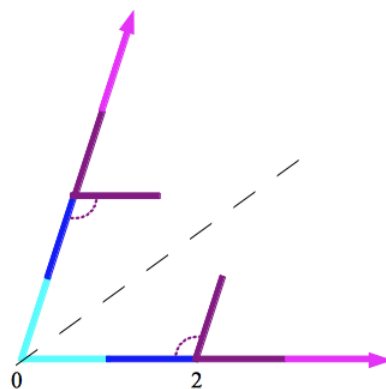
The additional constraint on growth can not be known by the system until a collision occurs. Therefore the initial formation is repeated at the new branch junctions.

Iteration #3



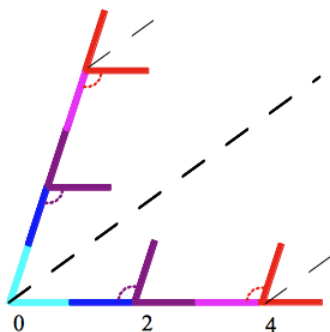
The last branch segment of the secondary branches produced at length 2 collide and are removed.

Iteration #3



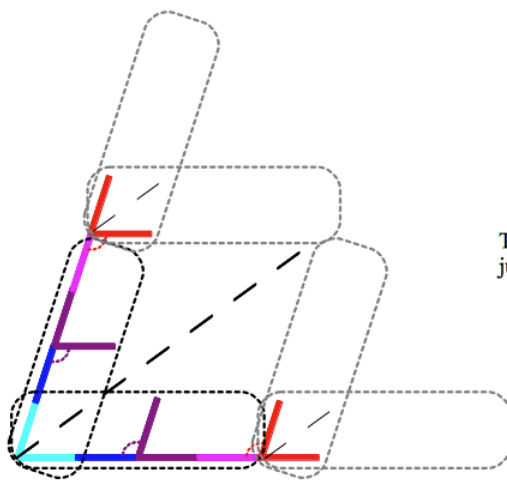
After a branch junction, the only branches which are moving forwards are the main branches (as shown in iteration #1)

Iteration #4



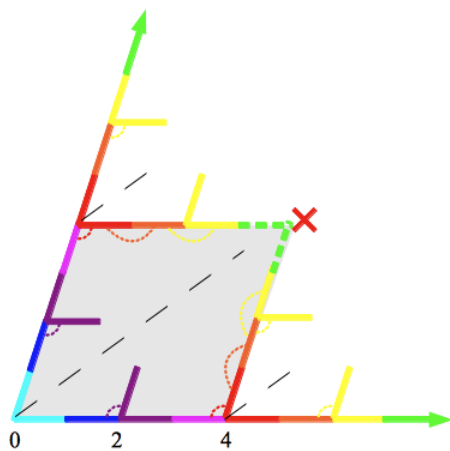
After a branch with no secondary branches is created, a branch junction can be formed (as in iteration #2). The constraints on the branch junction are the same as the initial branch junction with an additional constraint on the length of the secondary branch at iteration 4 to be < 4

Iteration #4



The structure is repeated at the new branch junctions.

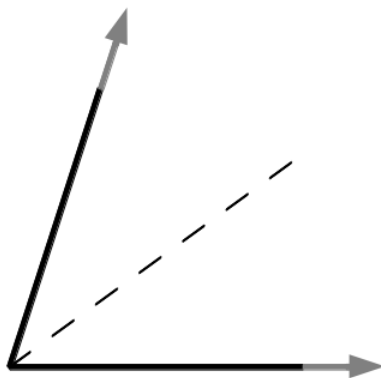
Iteration #7



The last branch segments on the secondary branches at length 4 are removed.

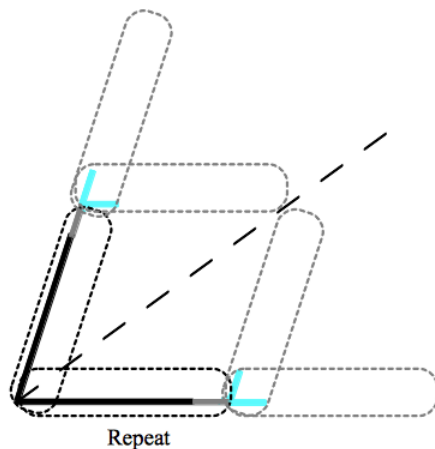
The only branches moving in the forwards direction are the main branches as the structure repeated this form.

Inductive step
Iteration
2^{n-1}



Assuming the system has continued as it did before, step 2^{n-1} has only the main branch moving in the forward direction and all other branch tips are terminated or moving backwards towards the structure.

Iteration
2^n



From a branch with no secondary branches, a new secondary branch is formed at iteration 2^n . The constraints on the new branch junctions are the same as the initial branch junction with an additional constraint on the length of the secondary branch at 2^n to be $< 2^n$ and thus the system repeats and removes the last branch segment at 2^n .

Step $2^{n+1}-1$ will have only the main branches moving forwards as this is a repeated form which takes us back to the previous inductive step.

The branching model presented starts with a single branching junction between two main branches. Each main branch extends by one unit resulting in a length of 2. The structure then repeats the entire formation on both main branch tips every 2^n iterations and removes the last branch segment of every secondary branch produced at 2^n , for arbitrary n .

The steps for growth in the branching structure are the same steps that can be used to produce a Sierpinski gasket and therefore the Sierpinski gasket will always be produced in this model of growth.

Returning to the sequence for the length of the longest secondary branches, “*highest power of 2 dividing $n - 1$* ”, we can start to understand now why this is so. If we add 1 to all the secondary branch lengths we get that the first secondary branch to be formed is of length 2. The next largest branch is twice this length, 4. The structure is then repeated to get branch lengths of, 2, 4, 2, 4, but the last branch length is doubled to get 2, 4, 2, 8. The next secondary branches then repeat this pattern again, 2, 4, 2, 8, 2, 4, 2, 8 and the last number is doubled, 2, 4, 2, 8, 2, 4, 2, 16 and so on. This is how the highest power of 2 dividing n is achieved in the model.

B.9 Discussion

A preliminary analysis into structural form from simple branching models was discussed. The model presented was able to produce intricate patterns with repetitive forms through interacting with other branches in the space and growing according to the amount of available space. Apparent self-similar behavior has been observed in the 2, 3 and 4-branch systems. Self-similarity for the 3 and 4-branch systems depends on the type of buds used or the role that the space around old branch tips that had branches removed is treated. This treatment can turn the 3 and 4 branch systems into alternating branching patterns or self-similar patterns. The 2-branch system is not affected by the treatment of past space as it is always moving in the forwards direction.

Further work not presented in this thesis has been done including preliminary analysis into the effect of adding rotations, a third dimension, randomness as well as looking into decreasing branch length to fit within the space and modeling branch-

ing structures in hyperbolic space. These results are unpolished and therefore not included in the thesis but further research includes analyzing the effect of different changes to the model on the resulting patterns in the hopes of understanding some generic properties of form from constrained growth. Determining different properties of these models would also be interesting along the lines of Holliday and Ulam who noted that the Ulam structure has only the main branches active every 2^n iterations [55].